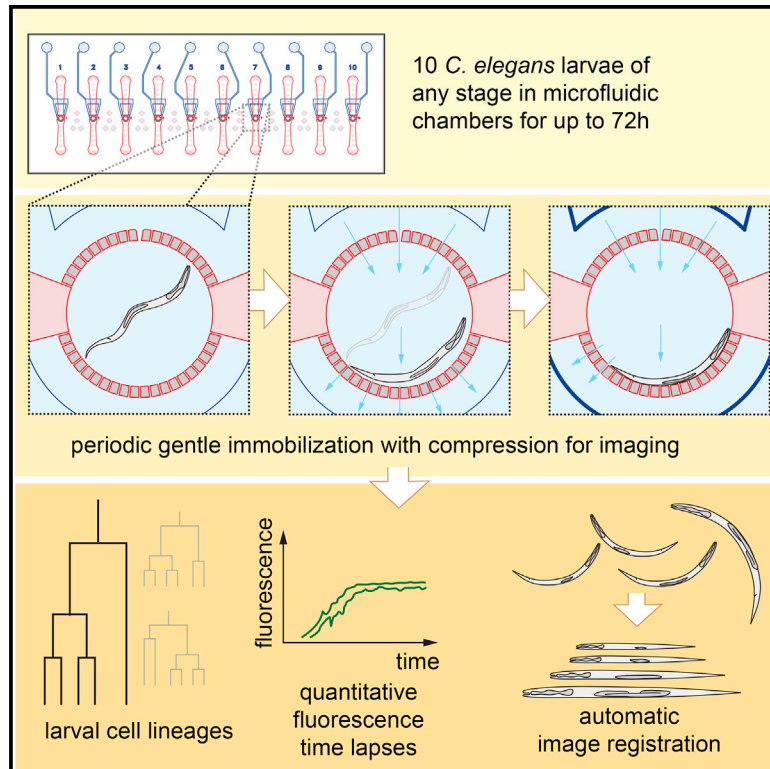


Developmental Cell

Long-Term High-Resolution Imaging of Developing *C. elegans* Larvae with Microfluidics

Graphical Abstract



Authors

Wolfgang Keil, Lena M. Kutscher,
Shai Shaham, Eric D. Siggia

Correspondence

wkeil@rockefeller.edu (W.K.),
shaham@rockefeller.edu (S.S.),
siggiae@rockefeller.edu (E.D.S.)

In Brief

Keil et al. present a microfluidics setup, enabling long-term, high-resolution, time-lapse microscopy of up to ten *C. elegans* larvae simultaneously. They collect vulval cell-cycle timing statistics, measure intensities of fluorescent transcriptional reporters during cell-fate specification, transdifferentiation, and cell death, and visualize complex neurite outgrowth in automatically registered z stacks.

Highlights

- Multichannel time-lapse imaging of *C. elegans* larvae of any stage for up to 72 hr
- Cell-cycle timing statistics of vulval lineages for >100 animals
- Fluorescent reporter expression during divisions, differentiation, and cell death
- Automated image registration enables visualizing complex neurite outgrowth



Long-Term High-Resolution Imaging of Developing *C. elegans* Larvae with Microfluidics

Wolfgang Keil,^{1,2,3,*} Lena M. Kutscher,² Shai Shaham,^{2,*} and Eric D. Siggia^{1,*}

¹Center for Physics and Biology

²Laboratory of Developmental Genetics

The Rockefeller University, New York, NY 10065, USA

³Lead Contact

*Correspondence: wkeil@rockefeller.edu (W.K.), shaham@rockefeller.edu (S.S.), siggiae@rockefeller.edu (E.D.S.)

<http://dx.doi.org/10.1016/j.devcel.2016.11.022>

SUMMARY

Long-term studies of *Caenorhabditis elegans* larval development traditionally require tedious manual observations because larvae must move to develop, and existing immobilization techniques either perturb development or are unsuited for young larvae. Here, we present a simple microfluidic device to simultaneously follow development of ten *C. elegans* larvae at high spatiotemporal resolution from hatching to adulthood (~3 days). Animals grown in microchambers are periodically immobilized by compression to allow high-quality imaging of even weak fluorescence signals. Using the device, we obtain cell-cycle statistics for *C. elegans* vulval development, a paradigm for organogenesis. We combine Nomarski and multichannel fluorescence microscopy to study processes such as cell-fate specification, cell death, and transdifferentiation throughout post-embryonic development. Finally, we generate time-lapse movies of complex neural arborization through automated image registration. Our technique opens the door to quantitative analysis of time-dependent phenomena governing cellular behavior during *C. elegans* larval development.

INTRODUCTION

The nematode *Caenorhabditis elegans* is optically transparent, exhibits an invariant cell lineage, and can be functionally probed using powerful genetic tools, making it a versatile setting for revealing principles of metazoan development. Studies of embryonic and larval *C. elegans* development have shed light on mechanisms driving cell-fate decisions, transdifferentiation, cell migration, and cell death; however, long-term high-resolution in vivo imaging of these processes has been accessible only in embryos (Bao et al., 2006; Du et al., 2014, 2015). Tracking cellular events in larvae usually requires tedious manual observations in which animals, mounted on agar pads affixed to glass slides, are imaged using fluorescence and/or differential interference contrast (DIC) microscopy (Sulston and Hodgkin, 1988;

Sulston and Horvitz, 1977). Live imaging often requires the addition of anesthetics to prevent animal motion, offering only ~3-hr imaging windows before viability is affected (Chai et al., 2012; Sulston and Hodgkin, 1988).

At 20°C, wild-type *C. elegans* larvae develop from hatching to adulthood in 50 hr (Hirsh et al., 1976). During this time, animals undergo molts defining four larval stages (L1–L4). L1 animals are 15 μm wide and 250 μm long, yet are flexible enough to squeeze through 5-μm channels (Aubry et al., 2015). L4 and adult animals are larger, typically 30–50 μm wide and 800–1,000 μm long, and are more resilient to harsh touch than L1 larvae. To progress through development, larvae require food for growth, and locomotion to shed and replace their cuticle at each molt. Automated methods for imaging larvae must, therefore, contend with larval size variation, and must allow sufficient locomotion for molting.

Several microfluidic platforms enabling larval imaging have been previously described. Most are designed for single short-term immobilization, and allow phenotypic characterization, laser microsurgery, and cell ablation (Ben-Yakar et al., 2009; Chokshi et al., 2009, 2010; Chronis et al., 2007; Chung et al., 2008; Kim et al., 2013; Rohde et al., 2007). Two methods have been proposed for long-term imaging. Hulme et al. (2010) designed a device for imaging from the L4 stage onward; however, L1–L3 animals cannot be immobilized in this setting. Krajniak and Lu (2010) proposed a device in which animals are immobilized by periodic immersion in a biocompatible polymer solution that undergoes a reversible temperature-dependent sol-gel transition, stiffening the animal at temperatures above the gelation temperature. Long-term imaging using this method requires temperature changes of 7°C to 10°C at the imaging frequency, altering the rate of *C. elegans* development, thus making comparisons between animals difficult. Furthermore, immobilized animals can freely rotate around their longitudinal axis, and this can be triggered by blue light often required for fluorescence imaging. As an alternative to microfluidics, Gritti et al. (2016) very recently proposed ultrafast imaging of moving larvae in microchambers. However, this technique requires custom-built microscopy equipment, allows for imaging of very bright fluorescent reporter signals only, and does not permit multichannel acquisitions.

Here we present a simple microfluidic platform for robust, long-term, high-resolution imaging of *C. elegans* through larval development. Ten animals, each confined by a circular array of posts, 4.88 μm apart, in a 400-μm diameter chamber, can be

imaged concurrently. Animals are gently immobilized by flow and gradually increasing pressure in a microfluidic layer on top of the growth chamber, and can be imaged hundreds of times from hatching to adulthood at frame rates <10 min, without apparent defects in the rate or fidelity of development. Our technique is compatible with all standard microscopy platforms, including scanning confocal microscopy.

Using our device, we statistically characterize cell-cycle parameters during *C. elegans* vulval development, a model system for cell-fate patterning and organogenesis. We combine DIC and fluorescence microscopy to follow cell-fate acquisition, cell migration, cell differentiation, and cell death. Finally, we use multichannel deconvolution microscopy to obtain high-resolution time-lapse data of dendritic arborization dynamics. We show that these data can be automatically computationally aligned to follow in vivo neurite outgrowth over extended periods of time (24 hr).

These studies demonstrate that our device allows quantitative exploration of cellular and subcellular events at very high temporal and spatial resolution at all stages of *C. elegans* larval development.

Design

We fabricated a two-layer microfluidic device permitting confinement, feeding, and repeated immobilization of *C. elegans* for imaging at all larval stages (Figures 1A and 1B; [Experimental Procedures](#)). Our design incorporates a two-layer polydimethylsiloxane (PDMS) “flow-control” channel architecture (Unger et al., 2000) previously used to transiently immobilize adult *C. elegans* (Chokshi et al., 2009; Gilleland et al., 2010). Animals trapped in small circular chambers (diameter 400 μm) on the bottom flow layer of the device are grown in liquid monoxenic medium ([Experimental Procedures](#)). Chambers are delimited by a circular array of posts, each 21 μm wide and separated by 4.88 μm (Figures 1A and 1B) with the exception of an inlet (10 μm wide) for introducing animals into each chamber (Figure 1B, bottom). The air-filled compression layer (height, 50 μm) is located above the flow layer and transmits pressure to a flexible 150- μm PDMS membrane separating the compression and flow layers. The flow layer height is only 20 μm , minimizing optical distortions at the interface between the PDMS posts and the liquid medium. Since this low chamber ceiling could damage L3 or older animals, the compression layer chamber above is kept under negative pressure (-5 psi), raising the chamber ceiling to >40 μm while animals are not immobilized (Figure 1B).

Unlike previously proposed devices, chamber inlets and outlets of our device are small enough to confine young larvae. In our hands, animals beyond the mid L2 stage never escaped the chambers during imaging, while L1 larvae escaped the chamber in $\sim 5\%$ of the imaged cases. We were able to easily load animals at all larval stages into the chambers without failures (see [Supplemental Detailed Protocol](#)) and the chamber itself is sufficiently large to comfortably host adults. Moreover, clogging of one or a few inlet channels of the chamber by contaminating particles only weakly alters the system flow properties, and does not disable the immobilization mechanism (see below; compare with Hulme et al., 2010).

To gently immobilize fragile young larva, we employ a two-step procedure (see [Movie S1](#)). First, we gradually apply increasing

negative pressure (maximum -4 to -16 psi) to the outlet of the flow layer (Figure 1C, left). This elicits increasing flow toward the outlet, pushing animals to the side of the chamber. At the same time, the negative pressure in the compression layer chamber is gradually released back to ambient pressure. Second, we gradually increase the pressure applied to the compression layer, deflecting the PDMS membrane toward the flow layer below (Figure 1C, right). The deflected membrane restricts the animal’s movement by pushing it toward the side of the chamber (Figures 1C [right] and 1D). Reliable immobilization is achieved 45–60 s from the start of the procedure. The graded pressure adjustments to the top and bottom layers proved critical for avoiding damage to the animals and animal confinement. Abrupt onset of flow through the chamber frequently results in suction of L1 and L2 animals between the circular array posts. Sudden pressure onset in the compression layer can lead to physical damage to the animals, particularly during molting.

Previous *C. elegans* microfluidic devices were fabricated by casting and curing PDMS on molds obtained by photolithography on silicon wafers, mostly using photosensitive epoxy (negative photoresist) (Chronis et al., 2007; Crane et al., 2012; Gilleland et al., 2010; Hulme et al., 2010; Rohde et al., 2007). However, our flow layer requires fine and deep features (channels 4.88 μm wide and 20 μm deep) that cannot be easily accommodated by these techniques. We also aimed to reuse molds many times. We therefore opted to physically etch the silicon with deep-reactive ion etching (DRIE), a standard method for engineering micromechanical systems (Franssila, 2010) (Figure S1).

The full microfluidic device consists of ten independent identical *C. elegans* chambers (Figure 1E). Automated immobilization, through electropneumatic regulators, and automated imaging are combined to acquire time-lapse images after loading animals into the chambers. Our setup consists of two vacuum and pressure circuits, controlling chambers 1, 3, ..., 9 and 2, 4, ..., 10 independently (Figure 1F). While chamber 1 is imaged (compression chamber fully pressurized) the immobilization procedure for chamber 2 is underway, and so forth. This allows imaging each chamber as frequently as every 4 min (see [Supplemental Detailed Protocol](#)), although we generally chose 8-min (or longer) imaging intervals to allow recovery and feeding of animals between immobilizations.

RESULTS

Animals Develop at Nearly Wild-Type Rates in the Device

To determine whether animals could be repeatedly immobilized and imaged through larval development without damage, we followed L1 starvation-arrested animals introduced into the device for 72 hr (Figure 2A; $n = 30$). Animals were immobilized every 8 min for 10 s for DIC imaging through 20 axial z slices. Device temperature was maintained at 20°C with a custom temperature-controlled stage inset and an objective cooling ring ([Experimental Procedures](#); Figure S2). We assessed animal development by scoring molt onsets and the timing of the first egg-laying event (Figure 2B). We found that developmental speed was $\sim 15\%$ slower compared with that reported previously for animals growing on NGM plates seeded with OP50 bacteria (Hirsh et al., 1976; Sulston and Hodgkin, 1988) at

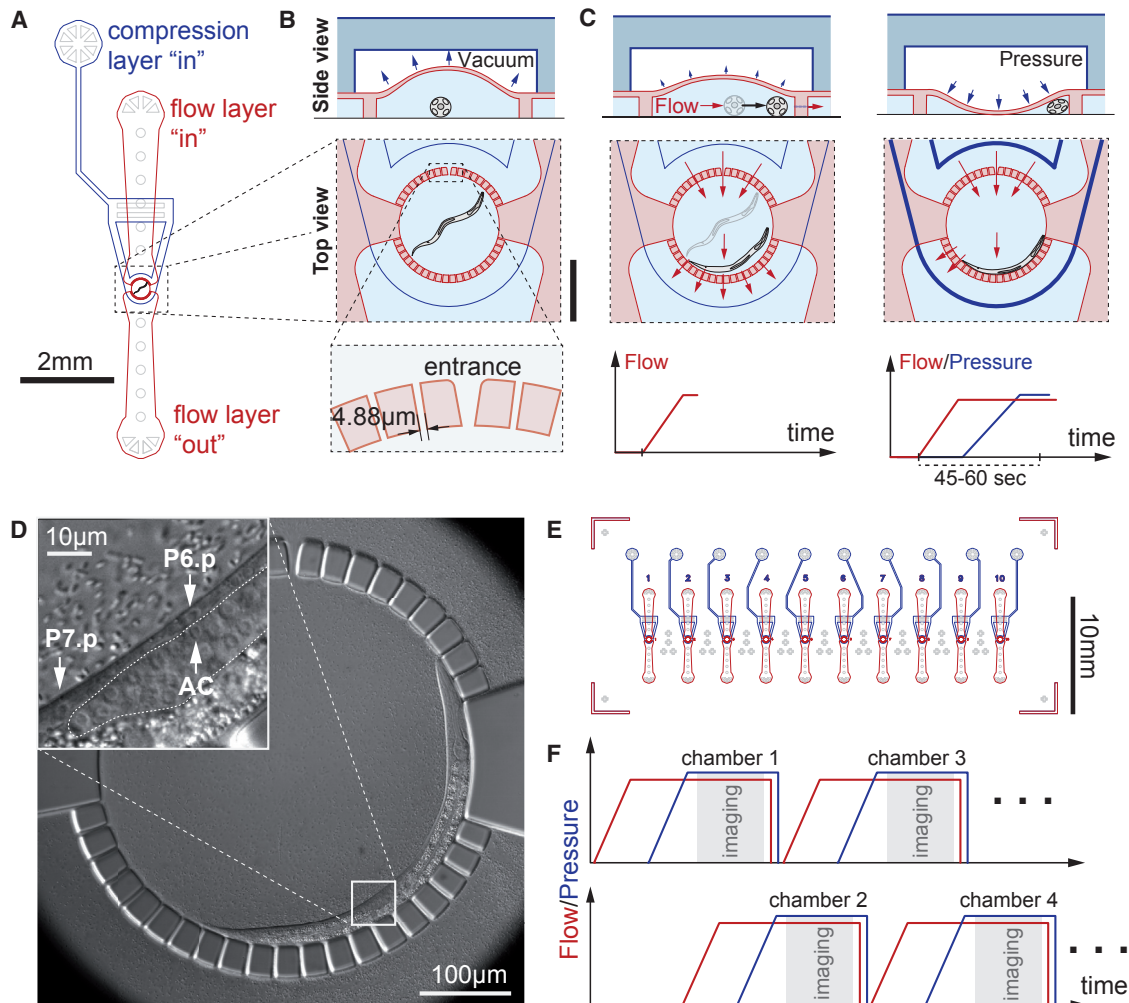


Figure 1. Device Layout and Operating Principle

(A) Schematic of a worm chamber with inlet and outlet ports for the flow layer (red) and the inlet port for the pressure layer (blue). Features in light gray are for structural support only.

(B) Side view (top) and top view (bottom) of a worm chamber. Scale bar 250 μm ; side view not drawn to scale. Height of the flow layer is 20 μm and height of the pressure layer chamber 50 μm . Top: between immobilizations, the pressure layer is kept under vacuum such that the height of the worm chamber is increased. Bottom: the animal is confined in the chamber through an array of posts with 4.88- μm spacing. Entrance to the chamber is 10 μm wide. The animal is drawn in cross-sectional view.

(C) Illustration of the immobilization procedure. Left: gradually increasing suction at the flow layer outlet (bottom) pushes the animal to the side of the chamber without flushing it through the small channels (top and middle). Right: vacuum in the pressure layer is gradually released and replaced by pressure. This slowly pushes down the membrane between the pressure and flow layers to gently compress and immobilize the worm.

(D) Differential interference contrast (DIC) image of an immobilized L2 larva in the chamber. Inset: Magnified view of the mid-body region. Arrows show nuclei of two vulval precursor cells (VPCs), P6.p and P7.p, as well as the anchor cell (AC). Dashed line indicates gonad outline.

(E) Illustration of the microfluidic chip with ten identical worm chambers. Features in light gray are for structural support.

(F) To achieve short imaging intervals, immobilization procedures and imaging for chambers 1, 3, ..., 9 and 2, 4, ..., 10 are staggered using two independent pressure/vacuum pipelines.

See also [Figures S1](#) and [S2](#).

20°C ([Figures 2A](#) and [2B](#)). However, egg laying in our device was synchronous with the plates, perhaps because the compression used for immobilization triggers premature egg laying. No animals died during imaging.

To probe the effects of repeated immobilization on development in more detail, we focused on development of the *C. elegans* egg-laying organ, the vulva. Synchronized L1 animals were grown for 22 hr outside the chip in liquid culture ([Experi-](#)

[mental Procedures](#)) until the mid to late L2 stage, when vulval precursor cells (VPCs) have completed ventral migration but have not yet divided. Animals were then either mounted into the device and immobilized and imaged every 8 min for 16 hr (120 immobilizations in total); mounted into the device, not immobilized, but similarly imaged; or kept in liquid culture for 16 hr ([Figure 2C](#)). Vulva morphology in the L4 stage was used as a precise indicator of overall developmental progression

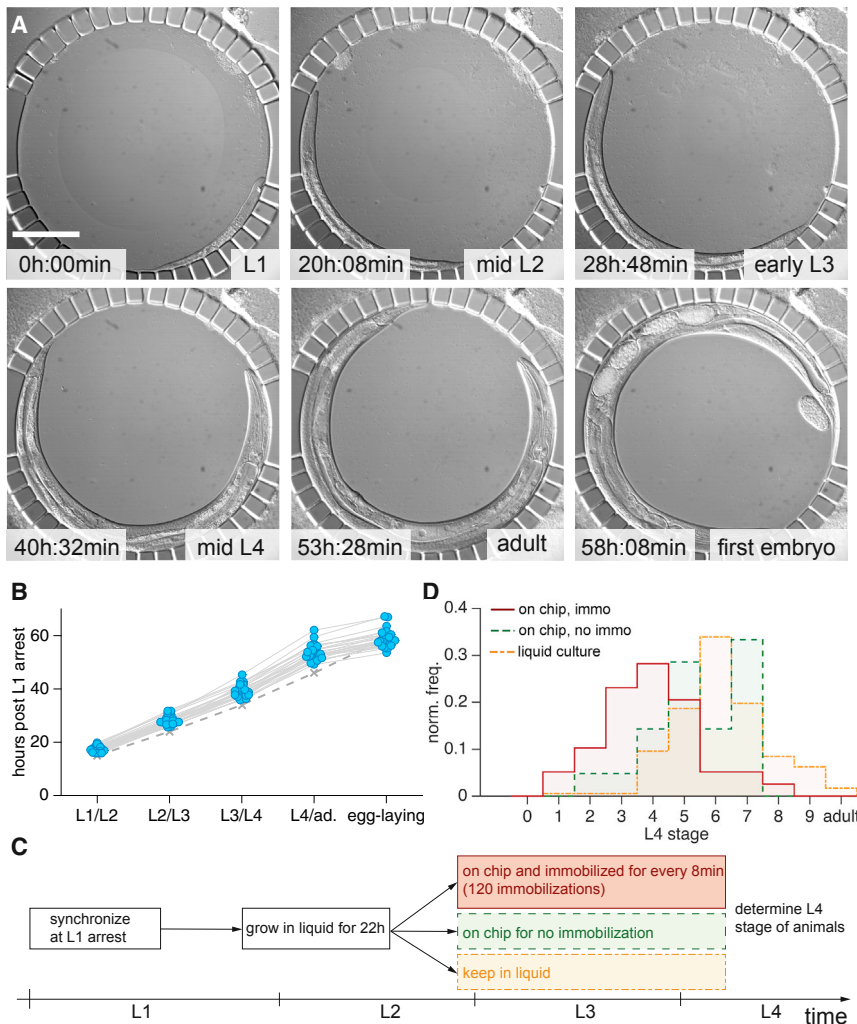


Figure 2. Developmental Timing Is Only Weakly Perturbed with Repeated Immobilization

(A) DIC micrographs of a developing larva in the worm chamber at different developmental stages between L1 (upper left) to the beginning of egg laying (lower right). Contamination at top right corner does not clog or alter device functionality. Scale bar, 100 μm .

(B) Molt times for 30 animals grown in the device from L1 arrest at 20°C. Solid gray lines connect time points of individual animals. Dashed gray line indicates data from Hirsh et al. (1976) under standard conditions on NGM petri dishes. Average time of L1 molt in device: 17 h 20 min (SD $\sigma = 1$ hr, 15 hr on NGM petri dishes; Hirsh et al., 1976); L2 molt: 28 hr ($\sigma = 1$ hr 40 min; 24 hr; Hirsh et al., 1976); L3 molt: 39 hr ($\sigma = 2$ hr 15 min; 39 hr; Hirsh et al., 1976); L4 molt: 53 hr 30 min ($\sigma = 3$ hr 46 min; 34 hr; Hirsh et al., 1976); Egg laying: 59 hr ($\sigma = 3$ hr 20 min, 59–60 hr; Hirsh et al., 1976).

(C) Experimental protocol to assess effects of repeated immobilization on developmental speed.

(D) Histogram of L4 developmental stages (Mok et al., 2015) after 38 hr of development post L1 arrest. Red, mounted into the device after 22 hr and immobilized and DIC imaged every 8 min (120 immobilizations, $n = 29$). Green, mounted into the device after 22 hr, DIC imaged but not immobilized ($n = 31$). Yellow, animals kept in liquid culture for 38 hr ($n = 177$).

(Mok et al., 2015). Animals in all three conditions entered the L4 stage and completed all vulval cell divisions (Figure 2D). Animals kept in liquid culture progressed, on average, through stage L4.6 (Mok et al., 2015), while animals kept in the device without immobilization reached the L4.5–L4.6 stage. Immobilized animals progressed, on average, through stage L4.4, a delay of only ~ 1.5 hr compared with freely moving animals. Importantly, the temporal spread of stage distributions was comparable under all three conditions. Thus, developmental variability was not increased by incubation in the device or by frequent immobilization.

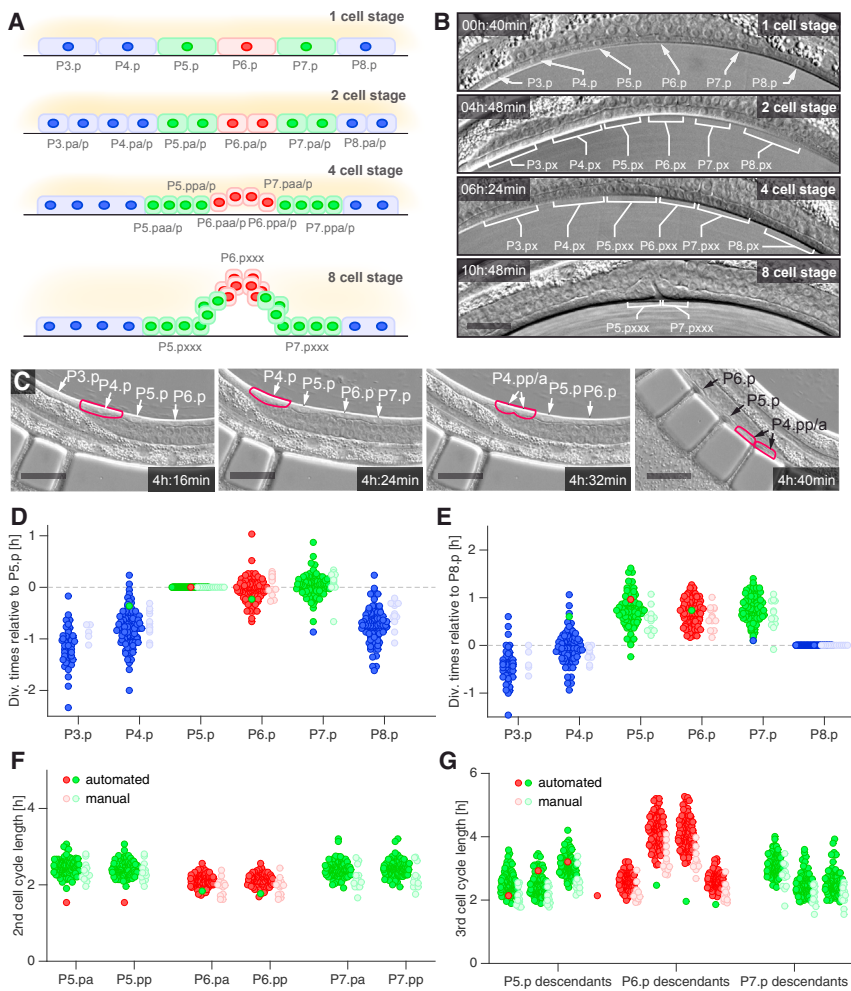
Statistical Power: VPC Cell-Cycle Onset and Duration during Vulval Development

To demonstrate the utility of our device for imaging larval cells at high temporal and spatial resolution in many animals, we collected cell-division timing data during *C. elegans* vulval development. Previous studies (Greenwald et al., 1983; Hulme et al., 2010; Sternberg and Horvitz, 1986; Sulston and Horvitz, 1977) demonstrated that the outer VPCs (P3.p, P4.p, and P8.p) divide once and fuse with the hypodermis (non-vulval 3° fate; P3.p divides in $\sim 50\%$ of animals) (Figures 3A and 3B). The inner VPCs (P5.p–P7.p), which eventually form the vulval opening (vulval

(along the left-right axis), requiring imaging through multiple focal planes. The time point during late metaphase/early anaphase when nuclei become featureless in DIC microscopy was used to score division times (Sulston and Horvitz, 1977).

Our microfluidics device enabled us to automatically obtain high-resolution DIC image stacks of each animal during vulval development (Figure 3B). We then scored VPC divisions (22 divisions/animal) with temporal precision of ~ 4 min by manually analyzing each 4D movie (10–15 min analysis time per animal) (Figure 3C and Movie S2).

During their first round of division, VPCs are arranged along the anterior-posterior (AP) axis at the very ventral side of the animal. When we immobilized worms in chambers with PDMS posts substantially higher than 20 μm , VPC divisions could not be scored reliably because of optical distortions at the PDMS to liquid medium interface. Importantly, however, with the current design, even when the ventral side of the animal is apposed to the PDMS posts, edge distortions are minor and VPC divisions can be scored with ease (see also Movie S2). We are able to readily score the final rounds of division, which are most challenging to image because of the small nuclei (2–3 μm) and transverse division axes (Movie S3).



(D–F) Cell-cycle statistics of VPC divisions. Dark red/green/blue circles indicate division times or cell-cycle length of $1^{\circ}/2^{\circ}/3^{\circ}$ fate cells, respectively, obtained by following divisions in the microfluidic device ($n = 106$ animals). Light red/green/blue circles indicate the same, except obtained through traditional lineaging ($n = 13$). Note that manual lineaging was performed at 23°C and cell-division times were rescaled to 20°C (see [Experimental Procedures](#) for details). (D) Time point of the first VPC division relative to the P5.p division in each animal. Note that in one animal, the anchor cell was misplaced anteriorly and P4.p–P6.p adopted vulval fates with cell-cycle timings indicative of cell fate. (E) As in (D) but relative to the P8.p division. (F) Length of the second VPC cell cycle. (G) Length of the third VPC cell cycle.

Using the obtained lineaging data, we quantified relative VPC division times as well as the durations of the second and third VPC cell cycles in wild-type animals ($n = 106$; [Figures 3D–3G](#)). As a control, we manually followed vulval development outside the device and scored VPC divisions times ($n = 13$). We found that cells adopting the non-vulval fate consistently divide earlier than vulval-fate cells. For example, P8.p divides 44 min earlier, on average, than P5.p. VPCs adopting the vulva fate undergo the first round of cell divisions more synchronously compared with non-vulval cells. The SD of the timing of the P6.p division relative to P5.p division, for example, is 12 min, compared with 20 min for P4.p relative to P8.p. Similar statistics were revealed in our manual lineaging experiments ([Figures 3D and 3E](#)).

The large number of lineaging experiments allowed us to define statistically significant trends in cell-cycle onsets and lengths during vulval development. For example, we can conclude that P7.p was more likely to divide last among P5–

Figure 3. Tracking Vulval Precursor Cell Divisions

(A) Cell divisions in *C. elegans* vulval development at the L3 stage. Dark ellipses indicate nuclei; brighter outlines indicate cell membranes. VPC progeny denoted by Pn.px where $n = 3, 4, \dots, 8$ and $x = a$ (anterior) or p (posterior) for the first two divisions. P6.p (red) executes the 1° fate (three rounds of cell divisions), P5.p and P7.p (green) execute the 2° fate (three rounds of cell divisions except P5.ppp and P7.paa). P3.p, P4.p, and P8.p (blue) divide once and fuse to the hypodermis (3° fate).

(B) DIC micrographs of 1-cell, 2-cell, 4-cell, and 8-cell stages of vulval development in a repeatedly immobilized larva. First two rounds of cell division for P5–7.p occur in the anterior-posterior orientation, giving rise to Pn.pxx (where $n = 5–7$; $x = a, p$). The terminal cell divisions of the P6.p granddaughters all occur in the transverse (left-right) orientation. The terminal cell divisions of P5.paa and P5.pap as well as P7.ppa and P7.ppp are longitudinal; P5.ppa and P7.pap undergo a final transverse division and P5.ppp and P7.paa do not divide further. P6.p descendants are outside of the focal plane of bottom panel. Scale bar, $20\ \mu\text{m}$.

(C) DIC micrographs of a P4.p cell division imaged at 8-min intervals. Purple outlines highlight P4.p and progeny. Left: P4.p nucleus and nucleolus are visible. Center left: Nuclear envelope breakdown has occurred, metaphase plate has formed, and no nuclear components can be seen. This is the most prominent feature of cell division in DIC microscopy and what is scored ([Sulston and Horvitz, 1977](#)). Center right: cytokinetic furrow is apparent by the kink on the ventral side of the cell (purple outline). Right: P4.p nuclei are visible. Division time would be scored as 4 h 24 min. Scale bar, $20\ \mu\text{m}$. See also [Movies S2 and S3](#).

7.p than P5.p and P6.p ($p < 0.01$, [Figure S3](#)) in contrast to previous reports using a much smaller sample size (see [Figure 1E](#) in [Nusser-Stein et al., 2012](#)). We also found that sister pairs of VPC daughters generally divide synchronously, and second VPC cell-cycle durations have narrow distributions ([Figure 3F](#)). Furthermore, P6.p always divided before P5/7.p (see [Figure S4](#)). The duration and variability of the second VPC cell cycle was almost identical to those obtained from manual observation (e.g., coefficient of variation for P6.p daughter cell-cycle lengths 0.10 versus 0.09 for manual versus automated imaging, respectively; see [Experimental Procedures](#)). Durations of the third cell cycle, particularly for innermost vulval cells, were more variable, both in our device and with manual lineaging ([Figure 3G](#)). We also found a significant positive correlation between the duration of the second and third cell cycles in individual animals, suggesting that variability in cell-cycle length may be developmentally controlled ([Figure S5](#)). Nonetheless, cell-cycle times are tightly associated with terminal cell fates.

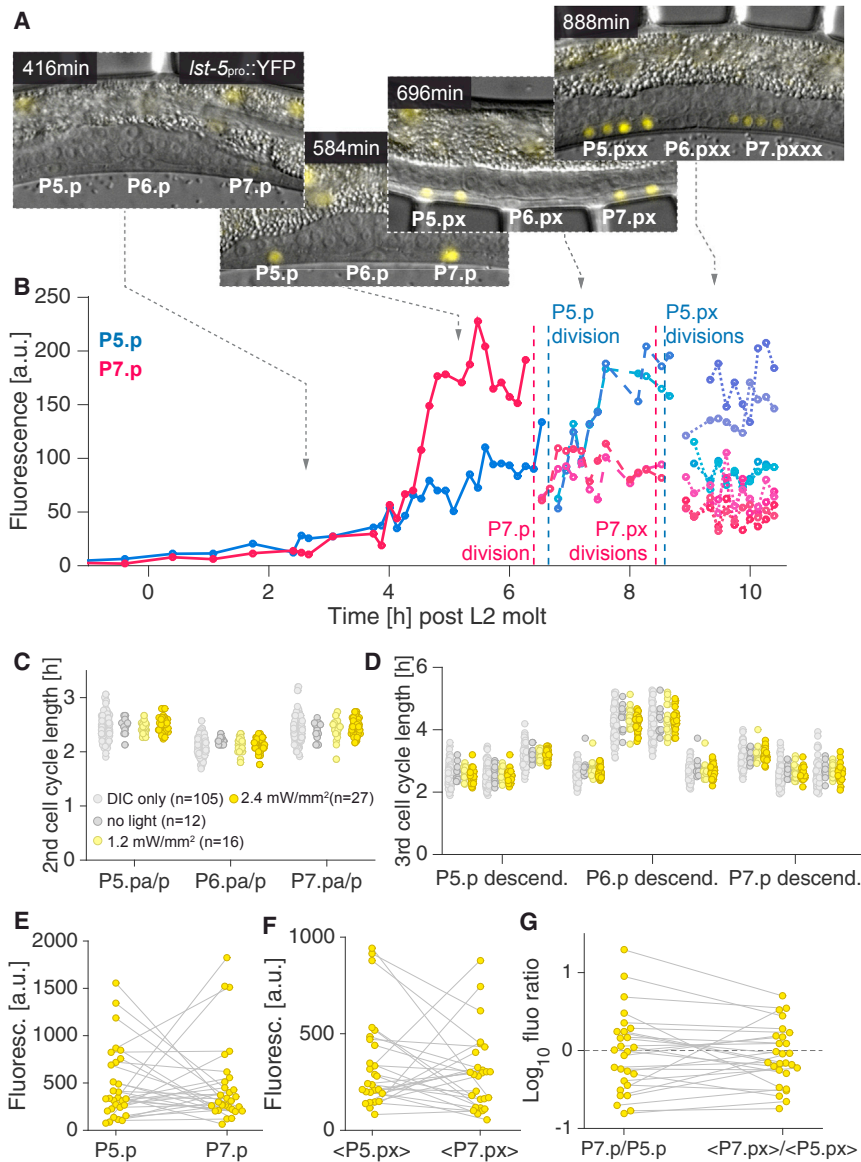


Figure 4. Time-Lapse Imaging of the Notch Target *Ist-5* during Vulval Induction and Development

(A) Merged DIC and fluorescence micrographs of a strain expressing the transgene *arl5116* (*Ist-5_{pro}::2xNLS::YFP*; *ceh-22::GFP*; *pha-1(+)*), a transcriptional reporter of Notch activity at different stages of vulval development, from the beginning of vulval induction (left) to the 4-cell stage (right, each vulval fate VPC divided twice) (3 ms/500 ms exposure DIC/YFP, 12 z slices, 1.5 μ m spacing).

(B) Fluorescence intensity as a function of time in P5.p/P7.p and their progeny (blue/red traces). Note that while Notch activity in P7.p is much stronger initially, daughters of P5.p show higher activity than daughters of P7.p.

(C and D) Length of second (C) and third (D) VPC cell cycle in P5–7.p as a function of light intensity used for epifluorescence imaging (510 nm, 25 nm excitation filter width).

(E) Fluorescence intensities of P5.p and P7.p (yellow circles) averaged over two imaging frames (16 min) prior to their respective first division. Gray lines connect values for P5.p and P7.p in the same animal ($n = 27$).

(F) As (E) but for daughter cell pairs P5.pa/p and P7.pa/p ($n = 27$). Values indicate fluorescence intensities averaged over two imaging frames prior to the respective cell's division and averaged over sister cell pairs.

(G) Fluorescence intensity ratios of P5.p versus P7.p and their respective daughter cell pairs. Gray lines connect values for VPCs and VPC daughters in the same animal ($n = 27$).

expressed in 2° VPCs (usually P5.p and P7.p) and their descendants (Karp and Greenwald, 2013). LIN-12/Notch signaling between VPCs is known to promote 1° and 2° cell-fate establishment (Félix, 2012); however, time-lapse data on LIN-12/Notch activation has not been published. We imaged wild-type

Our dataset is extensive enough to include a rare, single animal, in which the vulval-fate pattern was shifted anteriorly by one VPC, such that P4–P6.p now adopted vulval cell fates. Interestingly, relative timings of VPC divisions were shifted accordingly in this animal (Figure 3D). Our dataset also includes a single animal in which P9.p became part of the vulval competence group and divided.

Together, these studies reveal that our device can be used to collect statistics on the spatiotemporal aspects of vulval development with very high resolution.

Quantitative Temporal Dynamics of Gene Expression: Notch-Dependent Transcriptional Reporter Expression during Vulval Development

To demonstrate the use of our device in tracking variable gene expression patterns over time, we followed expression of *Ist-5*, a direct transcriptional target of LIN-12/Notch (Karp and Greenwald, 2013; Li and Greenwald, 2010; Yoo and Greenwald, 2005)

C. elegans expressing *Ist-5_{pro}::YFP* (see Experimental Procedures), and quantified fluorescence intensity over time from the late L2 stage until the 8-cell stage of vulval development in the late L3 stage (Figures 3A, 3B, 4A, and 4B). To ensure that vulval development was not perturbed by fluorescence imaging or prolonged immobilization, we performed two-channel (DIC/YFP) imaging of vulval development with different fluorescence light intensities (0 mW/mm² [$n = 12$], 1 mW/mm² [$n = 16$], 2.4 mW/mm² [$n = 27$]) and followed VPCs through their divisions (Figures 4A, 4C, and 4D). Exposures of 500 ms were used for each z slice to obtain quantifiable images, as *Ist-5::YFP* expression is weak. Immobilization times were therefore 20 s compared with 10 s for DIC microscopy only. Vulval development proceeded normally in all conditions, and cell-cycle durations were indistinguishable among animals exposed to fluorescence excitation and compared with animals imaged by DIC only (Figures 4C and 4D). Thus, neither longer immobilization periods nor the *Ist-5* reporter transgene affect vulval development.

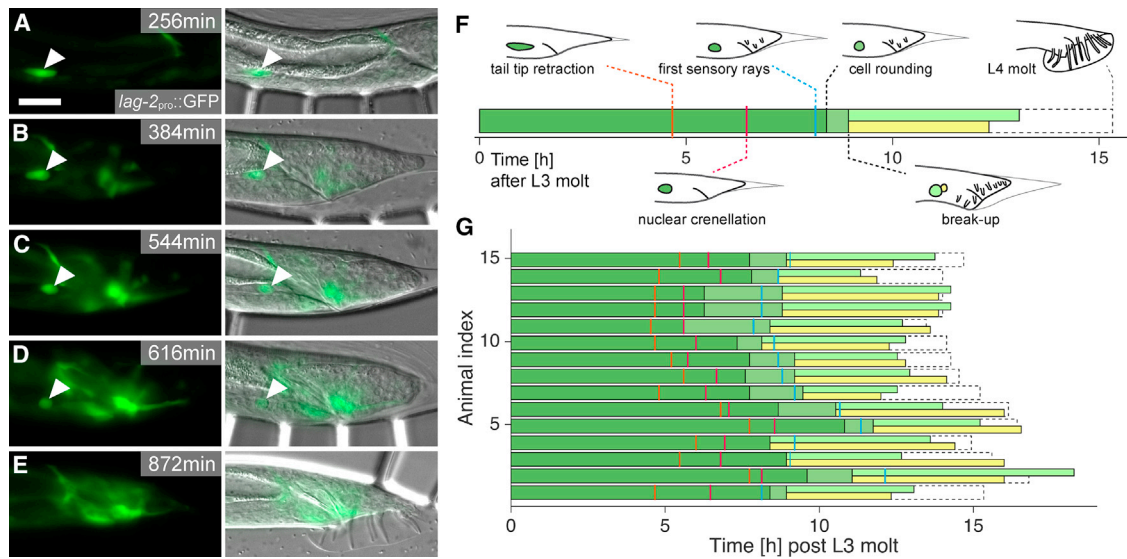


Figure 5. Tracking Non-apoptotic Linker Cell Death in the *C. elegans* Male

(A–E) Fluorescence (left) and merged DIC and fluorescence (right) micrographs of a strain expressing the transgene *qls56* (*lag-2_{pro}::GFP*; *unc-119(+)*) (3 ms/15 ms exposure DIC/GFP (1.2 W/mm²), 18 z slices, 1 μm spacing) at various L4 stages. White arrowheads denote linker cell (LC). Time from start of imaging indicated. Sensory rays are not visible because they are in different focal planes. Scale bar, 20 μm. (A) Early L4 stage prior to onset of tail-tip retraction. (B) Start of tail-tip retraction/end of LC migration. (C) Onset of LC rounding. (D) Breakup into two fragments during engulfment. (E) After L4 molt, both LC fragments are cleared.

(F) Schematic time course of male L4 development and hallmarks of LC death and tail morphology for the animal shown in (A) to (E). Dark green and green colors denote LC presence prior to and after cell rounding, respectively. Light green and yellow bars indicate the presence of the two LC fragments. Dashed outline indicates duration of the L4 stage.

(G) LC death progression and morphological features of male tail development (n = 15). Colors as in (F). The sequence of tail morphogenesis events and LC death hallmarks is stereotypic.

We quantified fluorescence as a function of time at 2.4 mW/mm² light intensity (n = 27) throughout vulval induction and during the first two rounds of VPC divisions (Figures 4B and 4E–4G). We found that expression of the *Ist-5_{pro}::YFP* Notch activity reporter is often surprisingly asymmetric, with one of the two 2^o fate VPCs sometimes exhibiting 10-fold higher fluorescence intensities than the other (Figures 4C and 4E–4G). P5.p and P7.p were equally likely to show stronger reporter expression (Figure 4E). Asymmetric reporter activity was also observed during the two-cell stage of vulval development (Figure 4F). In 9 out of 27 animals, daughters of the less bright VPC at the one-cell stage became the brighter pair of cells (Figures 4A and 4G). We observed no correlation between relative cell-division times and fluorescence intensity of individual VPCs (Figure S6). Whether the observed variability in *Ist-5* fluorescence is caused by variability in transgene expression or documents true variability in Notch pathway activation during vulval development is unclear.

Nonetheless, these results demonstrate the efficacy of our setup in following transiently expressed reporters during larval development, allowing quantitative assessment of dynamic changes in gene expression.

Imaging Linker Cell Death through the L4 Molt

Permanent immobilization of *C. elegans* for imaging can greatly perturb development and can lead to lethality. To demonstrate the utility of our device in imaging cellular events during developmentally sensitive periods, we followed linker cell (LC) devel-

opment. The LC is born in the L2 stage and leads elongation of the male gonad during the L3 and L4 stages (Schwarz et al., 2012). The cell undergoes non-apoptotic programmed cell death in the late L4 stage (Blum et al., 2012), and the genetic basis for this has been under recent investigation (Blum et al., 2012; Kinet et al., 2016). Live imaging of LC death has been a major challenge in the field, as imaging for >10 hr is required, often through the L4-adult molt. Previous attempts at animal immobilization during this period resulted in lethality, likely because of the inability of the animal to properly molt (L.M.K. and S.S., unpublished data). We used our device to obtain a time course of LC death progression relative to overall male tail development in animals expressing *lag-2_{pro}::GFP* (see Experimental Procedures), which brightly labels the LC through its migration and death (Figures 5A–5E). We found that changes in LC morphology could often be ordered with respect to morphological changes in tail development (Figures 5F and 5G): Tail-tip retraction is followed by LC nuclear crenellation, onset of sensory ray morphogenesis, LC rounding, breakup of the LC into two left-right fragments (see Abraham et al., 2007), degradation of both fragments; and the L4 molt. In 2 out of 17 cases, animals died in our device during the L4 molt, likely because the cuticle became entangled in the sensory rays, and flow pulling on the cuticle ripped the tail apart. These animals were excluded from our analysis. In conclusion, our microfluidic setup, allowing periodic release of imaged animals, enables previously inaccessible live imaging of larvae through developmentally sensitive periods.

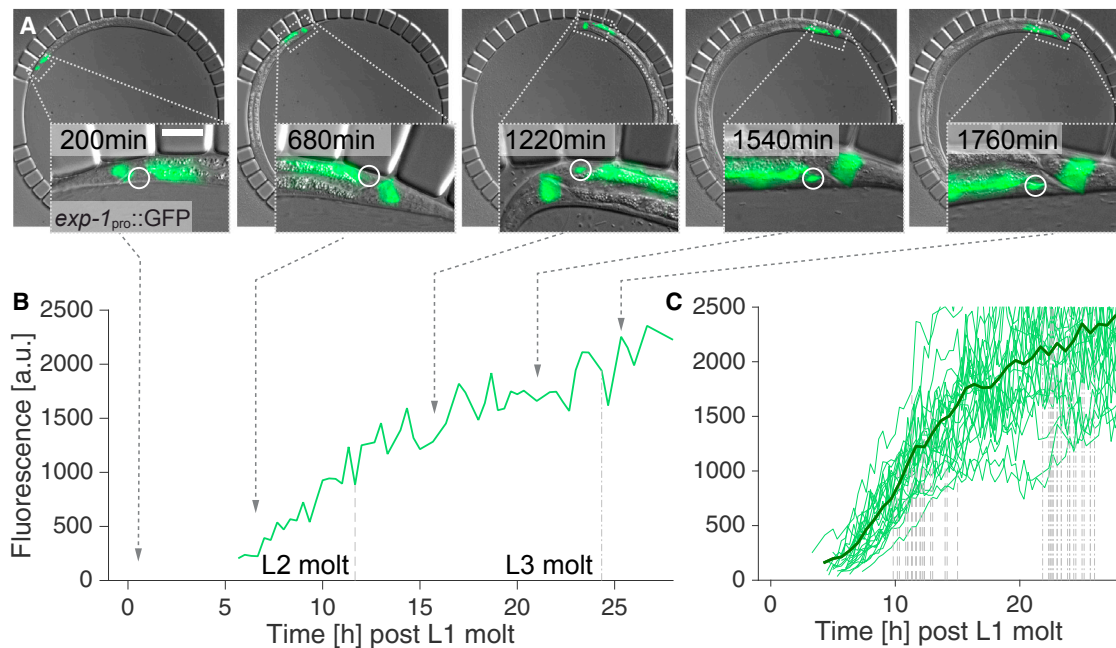


Figure 6. Y Cell/PDA Neuron Transdifferentiation

(A) Merged DIC and fluorescence micrographs of a wild-type larva expressing the transgene *ns131* (*exp-1_{pro}::GFP*). Insets show tail region of the animal, white outline indicates Y cell/PDA neuron position. Left: early L2 stage; middle left: mid L2 stage; middle: late L2 stage; middle right: mid L3 stage; rightmost: L3 molt (3 ms/25 ms exposure DIC/GFP [1.2 W/mm^2], 18 z slices, $1 \mu\text{m}$ spacing). Scale bar, $20 \mu\text{m}$.

(B) Time course of fluorescence intensity at the position of the Y cell/PDA neuron for the animal in (A). Dashed line marks time points of L2 molt; dotted-dashed line, L3 molt.

(C) Time course of fluorescence intensities at the position of the Y cell/PDA neuron for 25 animals. Dashed lines mark time points of L2 molt; dotted-dashed lines, L3 molt. Synchronous onset of *exp-1* expression is revealed after traces are aligned to the L1 molt.

Time-Lapse Imaging of Young Larvae: Y Cell to PDA Neuron Transdifferentiation

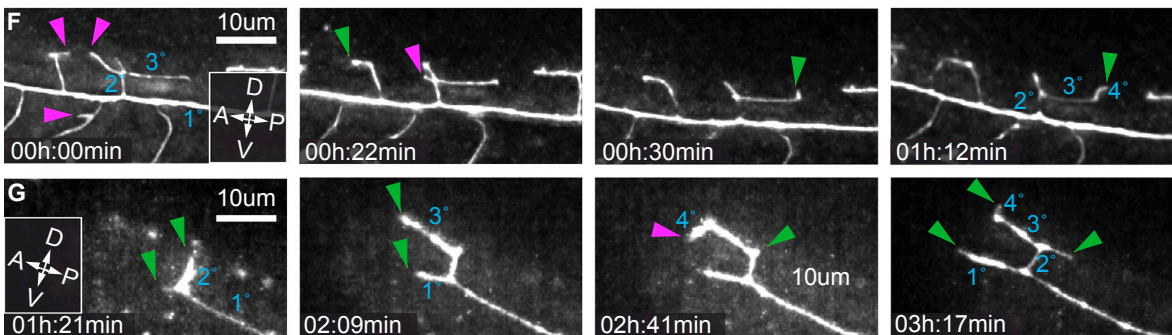
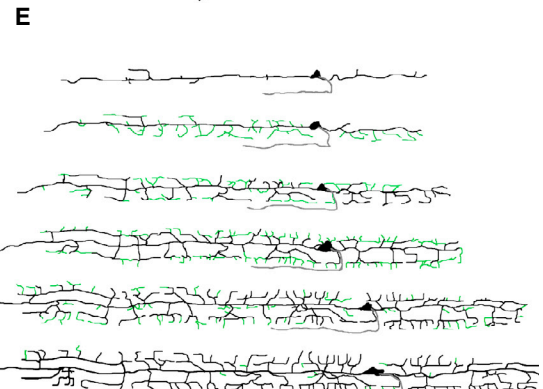
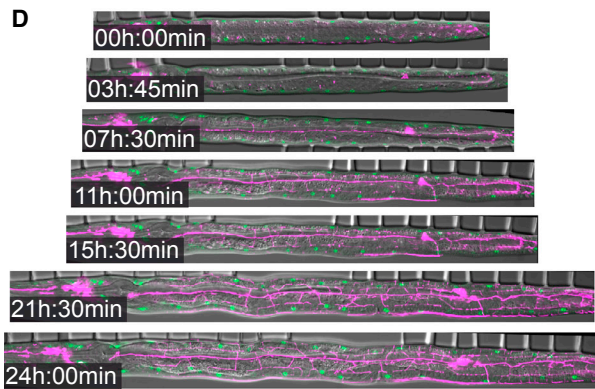
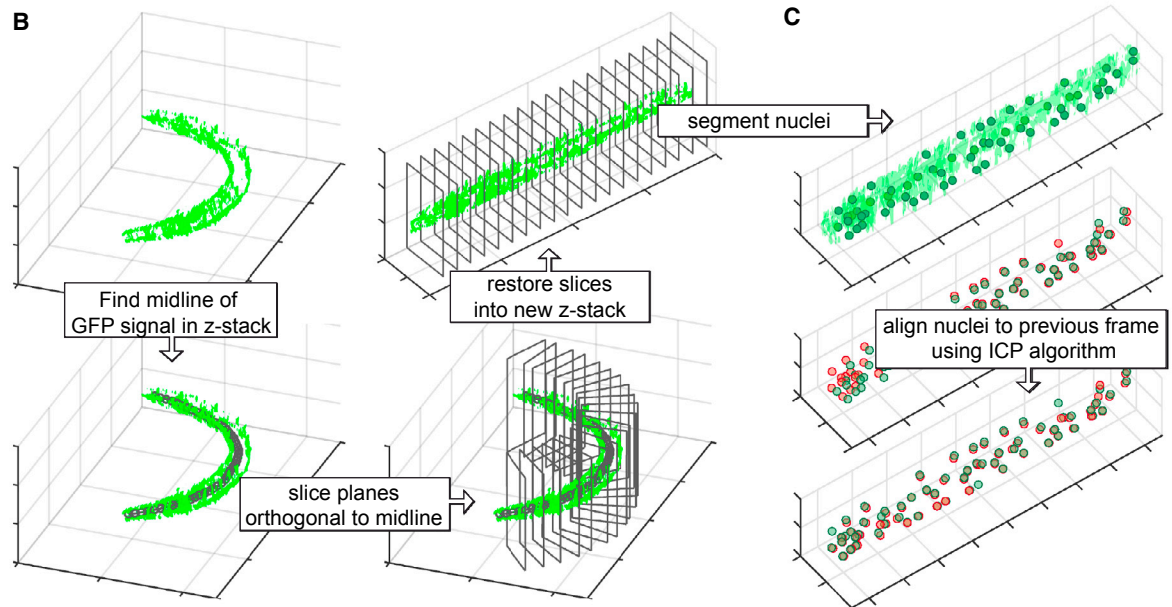
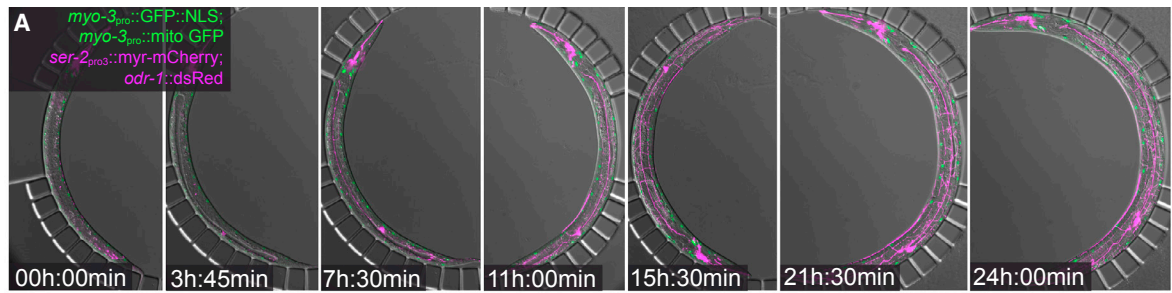
Imaging of young larvae has been a major challenge for *C. elegans* researchers. These animals are small and very sensitive to mechanical manipulation. To determine whether our device could be used for time-lapse imaging of developmental processes at these stages, we examined transdifferentiation of the epithelial Y cell into the PDA motor neuron. The Y cell is one of six cells of the *C. elegans* rectal epithelium. During late L1 the cell detaches from the epithelium, migrates anterodorsally (Jarriault et al., 2008; Sulston and Horvitz, 1977), and transdifferentiates into the PDA motor neuron, a cholinergic neuron that expresses the GABA receptor subunit EXP-1 (Beg and Jorgensen, 2003; Jarriault et al., 2008). Using our microfluidic device, we obtained time-lapse data on the Y cell/PDA neuron transition, starting from the onset of Y cell migration in L1 to the expression of the *exp-1* gene in the PDA neuron, as assessed by a transcriptional reporter ($>30 \text{ hr}$, $n = 25$) (Figures 6A and 6B, see Experimental Procedures). During the imaging, animals molted three times to reach the L4 stage. When aligned for the L1 molt, reporter expression dynamics were largely synchronous between animals, with detectable expression beginning 5 hr after the L1 molt, reaching saturation around the end of the L3 stage (Figure 6C).

These results demonstrate that our microfluidic device can be used for extended time-lapse imaging of cellular events that take place in young larvae.

Following PVD Neurite Outgrowth

C. elegans has emerged as a powerful model organism for understanding the principles of neural development. Importantly, substantial parts of the *C. elegans* adult neural circuitry are formed post-embryonically over periods of many hours (Hobert, 2010), and thus require long-term post-embryonic imaging for studies of in vivo neural circuit formation. Visualizing fine axonal and dendritic structure of *C. elegans* neurons requires high-resolution microscopy of often weak fluorescence signals. Our technique is particularly well suited to meet these requirements, even on wide-field imaging systems, as it enables gathering many z sections that yield confocal-like imaging quality after image restoration with deconvolution (Shaw, 2006).

To demonstrate these unique features and advantages of our approach, we performed long-term time-lapse imaging of PVD dendritic arborization, a prominent and spectacular example of post-embryonic neurite outgrowth in *C. elegans* (Figure 7A). PVD neurons are structurally, functionally, and molecularly similar to nociceptive neurons of more complex organisms (Smith et al., 2010; Wei et al., 2015; Yip and Heiman, 2016). The cell bodies of the two PVD neurons reside on either the right (PVDR) or left (PVDL) sides of the animal in posterior-lateral positions (Smith et al., 2010). The PVDs are born in the mid L2 stage, and immediately extend a single primary dendrite along the anteroposterior body axis. In their mature state (mid L4 stage), both neurons display a highly branched arbor of fine dendritic processes just beneath the epidermis of the animal,



(legend on next page)

covering most of the body. Previous time-lapse movies were performed exclusively with anesthetized animals, restricting imaging periods to between 30 min and 4 hr before animal viability was affected (Smith et al., 2010).

Using a fluorescent marker for the PVDs (*ser-2_{pro3}::myr-mCherry*; Yip and Heiman, 2016), we followed wild-type *C. elegans* from the late L2 to mid L4 stages (24 hr, time resolution 15 min), capturing nearly the entire phase of PVD dendritic arborization (Figure 7A). To render z stacks amenable to image restoration with deconvolution, we increased the z resolution to 0.7 μm , totaling 36 slices for each z stack. In addition to the mCherry marker for PVD, we also imaged a GFP marker for body wall muscle cells (*myo-3_{pro}::NLS::GFP*, *myo-3_{pro}::mito::GFP*; Liu et al., 2009), as well as DIC to monitor overall animal developmental progression (Figure 7A) (molts, vulval development, gonadal extension, etc.). All animals developed at wild-type rates during three-channel imaging sessions ($n = 17$), and immobilization was sufficient to obtain merged three-channel micrographs (Figure 7A). The *ser-2_{pro3}::myr-mCherry* reporter is first detected in early L3 animals, allowing visualization of PVD secondary (2°) branch formation and beyond to the fully branched pattern of quaternary (4°) dendrites (Smith et al., 2010) (Figure 7A).

Unlike the other studies we present here, which followed local cell groups, PVD neurons extend over the entire *C. elegans* body. Thus, spatial alignment of consecutive z stacks in time is essential for following PVD development. Therefore, we computationally aligned z stacks using automated segmentation of body wall muscle nuclei positions and DIC images, i.e., without using the mCherry reporter. The algorithm performs alignment in four steps (see Experimental Procedures for further details): First, the worm image is straightened (Figure 7B) through automated backbone detection based on the deconvolved GFP signal (Peng et al., 2008). Second, the positions of the body wall muscle nuclei are determined from the GFP signal through pixel classification and subsequent segmentation (Figure 7C, top). Third, the AP and dorsal-ventral (DV) body axes are determined by the positions of the body wall muscles (AP axis) and the DIC stacks (DV axis). Fourth, each straightened frame is aligned to the previous frame by aligning the body wall muscle nuclei positions with an

iterative closest point algorithm (Figure 7C, middle and bottom). By processing the obtained images with the algorithm outlined above, we were able to obtain time-lapse movies of PVD dendritic arborization in a fully automated fashion (Figure 7D and Movie S4). These movies follow the full PVD dendritic structures over almost the entire phase of PVD neurite outgrowth, showing the neuron dynamically adding 2° , 3° , and terminal 4° dendrites (Figures 7D and 7E; Movie S4).

Finally, we asked whether our microfluidics setup could be used to obtain time-lapse data of PVD branching dynamics at higher temporal resolution. We first tested whether animals could be immobilized for prolonged periods of time. We found that larvae at all stages fully recovered, even after being immobilized and imaged for up to 10 hr, and eventually started laying eggs in the device. However, development typically paused after 3–4 hr of immobilization, most likely because of starvation, as animals cease pharyngeal pumping while immobilized. This offered a typical imaging window of 3–4 hr, which is difficult to achieve with conventional immobilization with anesthetics (Chai et al., 2012). In fact, when we performed time-lapse imaging of PVD neurite outgrowth at high temporal resolution (60 s) using the *ser-2_{pro3}::myr-mCherry* marker during prolonged immobilizations, we were able to capture the full richness of previously reported neurite dynamics for PVD (Smith et al., 2010), such as self-avoidance, retraction, and regrowth (Figures 7F and 7G; Movies S5 and S6).

Together, these experiments further illustrate the versatility of our technique and open perspectives for longitudinal studies of post-embryonic neural development of *C. elegans*. Moreover, the automated alignment method lays the foundation for automated analysis of different aspects of *C. elegans* post-embryonic development.

DISCUSSION

Time-lapse imaging of developing *C. elegans* larvae at high temporal and spatial resolution is key for quantitative analyses and detailed morphogenetic studies of post-embryonic cell migration, division, death, and differentiation. A method that accommodates all larval stages and allows for acquiring high-quality

Figure 7. Following PVD Neurite Outgrowth with Automated Alignment and Segmentation of High-Resolution Three-Channel Z Stacks and in Animals Subjected to Prolonged Immobilizations

(A) Merged DIC and deconvoluted fluorescence micrographs (see Experimental Procedures) of a wild-type larva expressing the transgenes *wyls581* (*ser-2_{pro3}::mCherry*; *odr-1::dsRed*) (magenta) and *ccls4251* (*myo-3_{pro}::GFP::LacZ::NLS*; *myo-3_{pro}::mitochondrial GFP*) (green) between late L2 (leftmost) and mid L4 (rightmost) (3 ms/25 ms/75 ms exposure DIC/GFP [1.2 W/mm²]/mCherry [8 W/mm²], 35 z slices, 0.7 μm spacing). *ser-2_{pro3}::mCherry* labels both left and right PVD neurons as well as several chemosensory neurons in the head region. *myo-3_{pro}::GFP* labels all body wall muscle cells. mCherry (magenta) and GFP (green) signals show maximum z projections of the left side (10–15 slices) of the animal to depict PVDL and left body wall muscle cells only.

(B) Illustration of the algorithm to straighten *C. elegans* images, based on the *myo-3_{pro}::GFP* marker (see text and Experimental Procedures for details). Top left: 3D surface rendering of the GFP reporter signal. Bottom left: GFP reporter signal with automatically detected backbone. Bottom right: illustration of orthogonal slices along the backbone. Top right: straightened GFP reporter signal.

(C) Computational alignment of the body wall muscle cell nuclei positions of two subsequent imaging frames (see Experimental Procedures for details).

(D) Straightened merged DIC and deconvoluted fluorescence micrographs from (A) (see Movie S4 for a full time-lapse movie of the experiment).

(E) Tracings of PVD dendritic structure for the images in (D). Green traces indicate branches that were added since the previous time point shown. Gray traces indicate the PVD axon.

(F and G) Sequence of PVD neurite outgrowth at high temporal resolution during constant prolonged immobilization in the device (see text and Experimental Procedures for details). (F) Time-lapse deconvoluted fluorescence micrographs of PVD dendritic structure of a late L3 stage larva imaged with *ser-2_{pro3}::mCherry*, illustrating dynamic outgrowth (green arrowheads) and pruning (magenta arrowheads) of PVD secondary (2°), tertiary (3°), and quaternary (4°) dendrites (time resolution 60 s, 48 z slices, 0.7 μm spacing, maximum z-projection of 12 slices is shown). White arrows indicate anteroposterior (AP) and dorsoventral (DV) axis. See Movie S5 for a full time-lapse movie. (G) Time-lapse deconvoluted fluorescence micrographs of PVD dendritic structure of an early L3-stage larva imaged with *ser-2_{pro3}::mCherry*, illustrating dynamic outgrowth and pruning of the primary (1°) and secondary (2°) dendrites (time resolution 60 s, 48 z slices, 0.7 μm spacing, maximum z-projection of 15 slices is shown). See Movie S6 for a full time-lapse movie.

multichannel z stacks of fluorescent reporters and bright-field channels at high temporal resolution has been lacking from the arsenal of *C. elegans* tools.

Here we have presented an effective method for imaging *C. elegans* through larval development at up to 4-min intervals, imaging ten animals at once with diffraction-limited spatial resolution. The functionality of our setup incorporates aspects of previously described methods for short-term immobilization of *C. elegans* larvae and long-term imaging of adult development. However, several critical adjustments and improvements to existing devices have been made to allow reliable imaging at all larval stages. Animals are confined in chambers with much smaller flow channels than previously used. Channels in our device are fine-tuned to be narrow enough to constrain L1 larva, yet large enough to allow inflow of bacteria for feeding. Animal immobilization, for imaging at high spatial resolution, is achieved by gradual, rather than abrupt, changes in pressure and flow, allowing slow relaxation toward the immobilized position without damage. In fact, of >200 animals imaged in this study, fewer than 3% died. Finally, pressure and flow time courses are synchronized with imaging using a custom computer interface to optimize time resolution for simultaneous imaging of up to ten animals. Notably, this interface is independent of the underlying microscopy platform, making our approach adaptable to all commercial microscopes including scanning confocal microscopy devices.

Recently, long-term imaging of *C. elegans* larvae has been performed without animal immobilization (Gritti et al., 2016). Animals placed in sealed microchambers (no flow) are optically sectioned on a very fast custom-built microscope in less than 0.1 s, bypassing image blurring caused by animal motion. However, such fast imaging requires strong signals (or potentially damaging light intensities) to achieve the necessarily short exposure times, making imaging of weakly expressed fluorescent reporters impossible and limiting temporal resolution to 20 min before animal viability is affected (Gritti et al., 2016). For the same reason, 3D stacks with sufficient z resolution to allow image restoration via deconvolution cannot be obtained, which prevents resolving fine structures such as neuronal processes. Moreover, the lack of animal immobilization precludes superposition of multiple fluorescence or DIC channels. Similarly, moving animals cannot be imaged with scanning confocal microscopy. Thus, the microfluidics immobilization technique presented here offers several key advantages over rapid imaging, making it a versatile, flexible, and powerful approach.

Our method now opens the door to the exploration of many developmental phenomena previously inaccessible experimentally. For example, aberrations in developmental timing caused by cell-cycle or heterochronic mutants, conventionally studied by manual imaging, can now be quantified with relative ease and with much higher statistical power than was previously possible. Indeed, we generated statistics for cell-cycle parameters during *C. elegans* vulval development, which led us to suggest tight interplay between cell-cycle re-entry after precursor quiescence and precursor fate specification. Specifically, we showed that cells adopting the vulval fate divide later and more synchronously than non-vulval cells. Supporting this, we imaged a rare animal in which mispositioning of the EGF-secreting cell, the anchor cell, changed VPC fate specification. In this animal, division timings closely tracked new cell-fate as-

signments. Thus, as with early embryonic cell cycles (Bao et al., 2008), synchrony and asynchrony in vulval cell divisions, as well as cell-cycle lengths, are coupled to cell fate. We also documented onset of neuronal gene expression during an epithelial cell to neuron transdifferentiation event, demonstrating that this transition is temporally precise. Surprisingly, despite a nearly invariant cell lineage, we showed that *C. elegans* larval development displays variability in gene expression levels, timing of cell divisions, and relative timing of developmental events.

Our microfluidics setup is ideally suited for combining long-term imaging with experimental techniques to manipulate development at the level of cell signaling, gene expression, or protein degradation. For instance, animals can be immobilized once for several minutes to perform on-chip cell ablations, and subsequently imaged as described here. Cell-specific gene expression can be induced with timed heat shocks, e.g., through cell-specific rescue of heat-shock factor 1 mutants (Bacaj and Shaham, 2007), while imaging is under way. Complementarily, tissue-specific auxin-induced protein degradation (Zhang et al., 2015) can be controlled readily on-chip by delivering (and/or removing) auxin in solution during imaging. Such experiments will enable developmental studies in *C. elegans* larvae with high temporal resolution and control. The unearthing of unexplored phenomena combined with statistical power suggests that long-term live imaging of *C. elegans* larvae will contribute to our understanding of general mechanisms governing metazoan development at the cellular level.

Limitations

A limitation of our device is that it is not suitable for studying animals beyond egg laying or studying in utero embryonic development because (1) immobilization through compression triggers premature expulsion of embryos and (2) embryos and hatched larvae will accumulate in the chamber together with the parent animal.

EXPERIMENTAL PROCEDURES

C. elegans Methods and Strains

Strains were handled using standard methods (Brenner, 1974). Synchronized populations of L1-stage animals were obtained from cultures of gravid adults by bleaching with sodium hypochlorite solution and allowing embryos to hatch in M9 without food overnight at 20°C. To prepare animals for imaging of vulval development, we transferred synchronized L1 animals to monoxenic medium and incubated them on a shaker for 22 hr at 20°C before mounting animals into the device. For imaging LC death (or PDA neuron transdifferentiation), animals were incubated for 30 hr (or 12 hr) in monoxenic medium before mounting. To manually follow vulval development, we picked late L2-stage animals from NGM plates seeded with OP50 *Escherichia coli* and mounted them on slides with 2% agar pads seeded with a small spot of OP50 suspension (1–2 μL) (Sulston and Hodgkin, 1988). Manual lineaging was performed at 23°C. To compare cell-cycle times between manual lineaging and automated imaging, we scaled manually obtained values to presumptive 20°C values via an Arrhenius law extracted from the molting data at different temperatures in Hirsh et al. (1976) (scaling factor 1.24, see also Begasse et al., 2015).

We used transgenic strain GS5231 (expressing *arls116* (*lst-5_{pro}::2xNLS::YFP*; *ceh-22::GFP*; *pha-1(+)*) (Karp and Greenwald, 2013; Li and Greenwald, 2010) for imaging *lst-5* expression during vulval development, and strain OS238 (Abraham et al., 2007), expressing *qls56* (*lag-2_{pro}::GFP*; *unc-119(+)*), for following LC death. OS238 contains a *him-5(e1490)* mutation in the background which leads to a higher frequency of males. Strain OS2158 (expressing

nsls131 (*exp-1_{pro}::GFP*) was used to image Y cell/PDA neuron transdifferentiation. Germline injections were used to create extra-chromosomal arrays (Mello et al., 1991). For the *exp-1* reporter, a 3.5-kb fragment of the *exp-1* promoter was fused to GFP and injected at 50 ng/μL. Extra-chromosomal arrays were integrated by UV irradiation as previously described.

For following PVD dendritic arborization, we used a strain expressing *wyls581* (*ser-2_{pro3}::mCherry*; *odr-1::dsRed*) and *ccls4251* (*pSAK2 myo-3_{pro}::GFP::LacZ::NLS*; *pSAK4 myo-3_{pro}::mitochondrial GFP*; *dpy-20(+)*). Animals were incubated for 22 hr in monoxenic liquid medium before mounting.

Mold Fabrication

We designed the flow and compression layers of the microfluidic device in AutoCAD (Autodesk) (File S1). The compression layer design was sent to a mask-making service (www.fine-line-imaging.com), which provided a transparency mask at 50,800-dpi resolution. We created the master mold for the compression layer by spin coating at 1,300 rpm for 30 s (300 rpm/s acceleration; prespin: 500 rpm, 5 s, 100 rpm/s) and patterning the resulting 50-μm layer of SU-8-3025 photoresist (MicroChem) with the compression layer transparency on a bare silicon wafer (100 mm diameter, www.universitywafer.com, see Figure S1). Chrome masks and molds for the flow layer were fabricated at the Cornell Nanoscale Science and Technology Facility. The mold for the flow layer was fabricated by etching (DRIE, 20 μm) the mask pattern on a silicon wafer (Etch Tool; PlasmaTherm, Versaline; see Figure S1). We coated flow and compression layer molds by putting wafers next to 250 μL of trichloro(1H,1H,2H,2H-perfluorooctyl)silane (Sigma-Aldrich) in a 15-mL Falcon tube cap in a vacuum desiccator overnight. After coating with trichlorosilane we waited 2 days before chip fabrication, because animals tended to stick to PDMS when chips were fabricated immediately after coating.

Microfluidic Chip Fabrication

We spin-coated the flow layer mold with 21 g of PDMS prepolymer mixture (Sylgard 184, Dow Corning; 20:1) at 900 rpm (100 rpm/s) for 9 s without prespin (see Figure S1). We cast 45 g of PDMS mixture (5:1) onto the compression layer mold. We degassed both layers of PDMS for 20 min in a vacuum desiccator until all air bubbles disappeared, and then partially cured both layers for 25 min at 80°C. We peeled off the PDMS replica from the compression layer mold, cut out the individual compression layer component of each chip (six per mold) with a razor blade, and created inlet holes in each using a reusable biopsy punch (World Precision Instruments; inner diameter 0.5 mm, outer diameter 0.69 mm). Using a dissecting microscope, we aligned the compression layer components of each chip over the partially cured flow layer on the etched silicon mold. The two layers were bonded together by a 3-hr bake at 80°C. We then gently peeled the combined PDMS layers from the wafer surface and punched inlet and outlet holes. We treated the combined PDMS layers as well as a 22 × 60-mm #1.5 glass coverslip (Fisherbrand) with air plasma (30 W, 60 s) to activate both surfaces. Finally, we pressed the molded side of the combined PDMS layers onto a glass coverslip and completed bonding of the chip at 80°C overnight. After fabrication, microfluidic devices were kept under vacuum until use. We usually fabricated 18 devices per day, in parallel from three identical replicas of flow and control layer molds. The simplicity of our design (a single flow channel per chamber and no microfluidic valves) ensures that fabrication of devices is simple and that all chambers of the chip are functional for immobilization in nearly all of the devices. Each microfluidic device was used for a single experiment only.

Integrated Control of Microfluidic Valves

We used a custom-written MATLAB and Java graphical user interface to orchestrate the operation of electropneumatic regulators and electric valves with automated imaging. Electropneumatic pressure/vacuum regulators (SMC) and electronic valves (Pneumadyne) were operated through an Arduino microcontroller via MATLAB's ArduinoIO free add-on toolbox. We used the open-source platform μManager (Edelstein et al., 2014) to control the microscope (Zeiss AxioObserver.Z1, 40x 1.3NA oil immersion objective) and camera (CoolSnap HQ2 Photometrics or Andor Zyla sCMOS). This allowed for integrated control of microscopy and microfluidics to synchronize animal immobilization with imaging. μManager offers the advantage that it can be controlled through MATLAB and enables operation of our setup with almost all commercial microscopes. Source code can be provided upon request.

Temperature Control

To control temperature of the objective, we used an objective cooling ring (Pecon) which was temperature regulated by a water bath (Figure S2). After connecting the tubing to the microfluidic device (see Supplemental Detailed Protocol), the chip was placed in a custom-built aluminum holder, which was then positioned on a custom-built stage inset (Figure S2 and Supplemental Detailed Protocol), which was temperature controlled by a Peltier Element. CAD drawings for the stage inset can be provided upon request.

Imaging, Fluorescence Intensity Measurements, Deconvolution, and Automated Z Stack Alignment

Full details are given in Supplemental Experimental Procedures.

SUPPLEMENTAL INFORMATION

Supplemental Information includes Supplemental Experimental Procedures, six figures, one Supplemental Detailed Protocol, one Supplemental Data file, and six movies and can be found with this article online at <http://dx.doi.org/10.1016/j.devcel.2016.11.022>.

AUTHOR CONTRIBUTIONS

W.K. designed the microfluidic chip, built the setup, conducted the experiments, analyzed and interpreted the data, implemented the alignment algorithm, and wrote the paper. L.M.K. conducted and analyzed LC experiments. S.S. and E.D.S. designed the experiments, interpreted the data, and wrote the paper.

ACKNOWLEDGMENTS

We are grateful to A. Libchaber and A. Brinvalou for the use of their laboratory facilities for microfabrication and computing and to A. Petroff for help with photolithography and soft lithography. We thank members of the Shaham laboratory for discussions and insightful comments on the manuscript. Parts of this work were performed at the Cornell NanoScale Facility (CNF), a member of the National Nanotechnology Coordinated Infrastructure (NNCI), which is supported by the National Science Foundation (grant ECCS-1542081). We are particularly grateful to M. Skvarla (CNF) for providing the DRIE silicon wafer molds. Some strains were provided by the CGC, which is funded by NIH Office of Research Infrastructure Programs (P40 OD010440). We thank Iva Greenwald, Cori Bargmann, Hannes Buelow, and Kang Shen for sharing strains. This work was supported by a postdoctoral fellowship (LT000250/2013-C) from the Human Frontier Science Program (HFSP) Organization to W.K., NRSA Training Grant GM066699 to L.M.K., NSF grant PHY 1502151 to E.D.S., and NIH grants NS081490, HD078703, and NS064273 to S.S.

Received: June 1, 2016

Revised: October 24, 2016

Accepted: November 22, 2016

Published: December 29, 2016

REFERENCES

- Abraham, M.C., Lu, Y., and Shaham, S. (2007). A morphologically conserved nonapoptotic program promotes linker cell death in *Caenorhabditis elegans*. *Dev. Cell* 12, 73–86.
- Aubry, G., Zhan, M., and Lu, H. (2015). Hydrogel-droplet microfluidic platform for high-resolution imaging and sorting of early larval *Caenorhabditis elegans*. *Lab. Chip* 15, 1424–1431.
- Bacaj, T., and Shaham, S. (2007). Temporal control of cell-specific transgene expression in *Caenorhabditis elegans*. *Genetics* 176, 2651–2655.
- Bao, Z., Murray, J.I., Boyle, T., Ooi, S.L., Sandel, M.J., and Waterston, R.H. (2006). Automated cell lineage tracing in *Caenorhabditis elegans*. *Proc. Natl. Acad. Sci. USA* 103, 2707–2712.
- Bao, Z., Zhao, Z., Boyle, T.J., Murray, J.I., and Waterston, R.H. (2008). Control of cell cycle timing during *C. elegans* embryogenesis. *Dev. Biol.* 318, 65–72.

- Beg, A.A., and Jorgensen, E.M. (2003). EXP-1 is an excitatory GABA-gated cation channel. *Nat. Neurosci.* **6**, 1145–1152.
- Begasse, M.L., Leaver, M., Vazquez, F., Grill, S.W., and Hyman, A.A. (2015). Temperature dependence of cell division timing accounts for a shift in the thermal limits of *C. elegans* and *C. briggsae*. *Cell Rep.* **10**, 647–653.
- Ben-Yakar, A., Chronis, N., and Lu, H. (2009). Microfluidics for the analysis of behavior, nerve regeneration, and neural cell biology in *C. elegans*. *Curr. Opin. Neurobiol.* **19**, 561–567.
- Blum, E.S., Abraham, M.C., Yoshimura, S., Lu, Y., and Shaham, S. (2012). Control of nonapoptotic developmental cell death in *Caenorhabditis elegans* by a polyglutamine-repeat protein. *Science* **335**, 970–973.
- Brenner, S. (1974). The genetics of *Caenorhabditis elegans*. *Genetics* **77**, 71–94.
- Chai, Y., Li, W., Feng, G., Yang, Y., Wang, X., and Ou, G. (2012). Live imaging of cellular dynamics during *Caenorhabditis elegans* postembryonic development. *Nat. Protoc.* **7**, 2090–2102.
- Chokshi, T.V., Ben-Yakar, A., and Chronis, N. (2009). CO₂ and compressive immobilization of *C. elegans* on-chip. *Lab. Chip* **9**, 151–157.
- Chokshi, T.V., Bazopoulou, D., and Chronis, N. (2010). An automated microfluidic platform for calcium imaging of chemosensory neurons in *Caenorhabditis elegans*. *Lab. Chip* **10**, 2758–2763.
- Chronis, N., Zimmer, M., and Bargmann, C.I. (2007). Microfluidics for in vivo imaging of neuronal and behavioral activity in *Caenorhabditis elegans*. *Nat. Methods* **4**, 727–731.
- Chung, K., Crane, M.M., and Lu, H. (2008). Automated on-chip rapid microscopy, phenotyping and sorting of *C. elegans*. *Nat. Methods* **5**, 637–643.
- Crane, M.M., Stirman, J.N., Ou, C.-Y., Kurshan, P.T., Rehg, J.M., Shen, K., and Lu, H. (2012). Autonomous screening of *C. elegans* identifies genes implicated in synaptogenesis. *Nat. Methods* **9**, 977–980.
- Du, Z., Santella, A., He, F., Tionson, M., and Bao, Z. (2014). De novo inference of systems-level mechanistic models of development from live-imaging-based phenotype analysis. *Cell* **156**, 359–372.
- Du, Z., Santella, A., He, F., Shah, P.K., Kamikawa, Y., and Bao, Z. (2015). The regulatory landscape of lineage differentiation in a metazoan embryo. *Dev. Cell* **34**, 592–607.
- Edelstein, A.D., Tsuchida, M., Amodaj, N., Pinkard, H., Vale, R.D., and Stuurman, N. (2014). Advanced methods of microscope control using μ Manager software. *J. Biol. Methods* **1**.
- Félix, M.-A. (2012). *Caenorhabditis elegans* vulval cell fate patterning. *Phys. Biol.* **9**, 045001.
- Franssila, S. (2010). Etching. In *Introduction to Microfabrication*, S. Franssila, ed. (John Wiley & Sons), pp. 127–142.
- Gilleland, C.L., Rohde, C.B., Zeng, F., and Yanik, M.F. (2010). Microfluidic immobilization of physiologically active *Caenorhabditis elegans*. *Nat. Protoc.* **5**, 1888–1902.
- Greenwald, I.S., Sternberg, P.W., and Horvitz, H.R. (1983). The *lin-12* locus specifies cell fates in *Caenorhabditis elegans*. *Cell* **34**, 435–444.
- Gritti, N., Kienle, S., Filina, O., and van Zon, J.S. (2016). Long-term time-lapse microscopy of *C. elegans* post-embryonic development. *Nat. Commun.* **7**, 12500.
- Hirsh, D., Oppenheim, D., and Klass, M. (1976). Development of the reproductive system of *Caenorhabditis elegans*. *Dev. Biol.* **49**, 200–219.
- Hobert, O. (2010). Neurogenesis in the nematode *Caenorhabditis elegans*. *WormBook*, 1–24.
- Hulme, S.E., Shevkopyas, S.S., McGuigan, A.P., Apfeld, J., Fontana, W., and Whitesides, G.M. (2010). Lifespan-on-a-chip: microfluidic chambers for performing lifelong observation of *C. elegans*. *Lab. Chip* **10**, 589–597.
- Jarriault, S., Schwab, Y., and Greenwald, I. (2008). A *Caenorhabditis elegans* model for epithelial-neuronal transdifferentiation. *Proc. Natl. Acad. Sci. USA* **105**, 3790–3795.
- Karp, X., and Greenwald, I. (2013). Control of cell-fate plasticity and maintenance of multipotency by DAF-16/FoxO in quiescent *Caenorhabditis elegans*. *Proc. Natl. Acad. Sci. USA* **110**, 2181–2186.
- Kim, E., Sun, L., Gabel, C.V., and Fang-Yen, C. (2013). Long-term imaging of *Caenorhabditis elegans* using nanoparticle-mediated immobilization. *PLoS One* **8**, e53419.
- Kinet, M.J., Malin, J.A., Abraham, M.C., Blum, E.S., Silverman, M.R., Lu, Y., and Shaham, S. (2016). HSF-1 activates the ubiquitin proteasome system to promote non-apoptotic developmental cell death in *C. elegans*. *Elife* **5**.
- Krajniak, J., and Lu, H. (2010). Long-term high-resolution imaging and culture of *C. elegans* in chip-gel hybrid microfluidic device for developmental studies. *Lab. Chip* **10**, 1862–1868.
- Li, J., and Greenwald, I. (2010). LIN-14 inhibition of LIN-12 contributes to precision and timing of *C. elegans* vulval fate patterning. *Curr. Biol.* **20**, 1875–1879.
- Liu, X., Long, F., Peng, H., Aerni, S.J., Jiang, M., Sánchez-Blanco, A., Murray, J.I., Preston, E., Mericle, B., Batzoglou, S., et al. (2009). Analysis of cell fate from single-cell gene expression profiles in *C. elegans*. *Cell* **139**, 623–633.
- Mello, C.C., Kramer, J.M., Stinchcomb, D., and Ambros, V. (1991). Efficient gene transfer in *C. elegans*: extrachromosomal maintenance and integration of transforming sequences. *EMBO J.* **10**, 3959–3970.
- Mok, D.Z.L., Sternberg, P.W., and Inoue, T. (2015). Morphologically defined sub-stages of *C. elegans* vulval development in the fourth larval stage. *BMC Dev. Biol.* **15**, 26.
- Nusser-Stein, S., Beyer, A., Rimann, I., Adamczyk, M., Piterman, N., Hajnal, A., and Fisher, J. (2012). Cell-cycle regulation of NOTCH signaling during *C. elegans* vulval development. *Mol. Syst. Biol.* **8**, 618.
- Peng, H., Long, F., Liu, X., Kim, S.K., and Myers, E.W. (2008). Straightening *Caenorhabditis elegans* images. *Bioinformatics* **24**, 234–242.
- Rohde, C.B., Zeng, F., Gonzalez-Rubio, R., Angel, M., and Yanik, M.F. (2007). Microfluidic system for on-chip high-throughput whole-animal sorting and screening at subcellular resolution. *Proc. Natl. Acad. Sci. USA* **104**, 13891–13895.
- Schwarz, E.M., Kato, M., and Sternberg, P.W. (2012). Functional transcriptomics of a migrating cell in *Caenorhabditis elegans*. *Proc. Natl. Acad. Sci. USA* **109**, 16246–16251.
- Shaw, P.J. (2006). Comparison of widefield/deconvolution and confocal microscopy for three-dimensional imaging. In *Handbook of Biological Confocal Microscopy*, J.B. Pawley, ed. (Springer), pp. 453–467.
- Smith, C.J., Watson, J.D., Spencer, W.C., and O'Brien, T. (2010). Time-lapse imaging and cell-specific expression profiling reveal dynamic branching and molecular determinants of a multi-dendritic nociceptor in *C. elegans*. *Dev. Biol.* **345**, 18–33.
- Sternberg, P.W., and Horvitz, H.R. (1986). Pattern formation during vulval development in *C. elegans*. *Cell* **44**, 761–772.
- Sulston, J.E., and Hodgkin, J. (1988). Methods. In *The Nematode *Caenorhabditis elegans**, W.B. Wood, ed. (Cold Spring Harbor Laboratory Press), pp. 587–606.
- Sulston, J.E., and Horvitz, H.R. (1977). Post-embryonic cell lineages of the nematode, *Caenorhabditis elegans*. *Dev. Biol.* **56**, 110–156.
- Unger, M.A., Chou, H.P., Thorsen, T., Scherer, A., and Quake, S.R. (2000). Monolithic microfabricated valves and pumps by multilayer soft lithography. *Science* **288**, 113–116.
- Wei, X., Howell, A.S., Dong, X., Taylor, C.A., Cooper, R.C., Zhang, J., Zou, W., Sherwood, D.R., Shen, K., and Davis, G.W. (2015). The unfolded protein response is required for dendrite morphogenesis. *Elife* **4**, e06963.
- Yip, Z.C., and Heiman, M.G. (2016). Duplication of a single neuron in *C. elegans* reveals a pathway for dendrite tiling by mutual repulsion. *Cell Rep.* **15**, 2109–2117.
- Yoo, A.S., and Greenwald, I. (2005). LIN-12/Notch activation leads to microRNA-mediated down-regulation of Vav in *C. elegans*. *Science* **310**, 1330–1333.
- Zhang, L., Ward, J.D., Cheng, Z., and Dernburg, A.F. (2015). The auxin-inducible degradation (AID) system enables versatile conditional protein depletion in *C. elegans*. *Development* **142**, 4374–4384.

Developmental Cell, Volume 40

Supplemental Information

**Long-Term High-Resolution Imaging of Developing
C. elegans Larvae with Microfluidics**

Wolfgang Keil, Lena M. Kutscher, Shai Shaham, and Eric D. Siggia

Inventory of Supplemental Materials

Supplementary Experimental Procedures

Figure S1, related to Figure 1. Illustration of the mold and chip fabrication processes

Figure S2, related to Figure 1. Temperature-controlled stage and setup.

Figure S3, related to Figure 3. Statistics of division orders for the first VPC division.

Figure S4, related to Figure 3.

Figure S5, related to Figure 3. Correlations between second and third VPC cell cycle durations.

Figure S6, related to Figure 4. Relative timing of the first division of P7.p vs. P5.p vs. fluorescence intensity ratio of P7.p vs. P5.p in animals expressing *Ist-5_{pro}::YFP*

Supplementary Movie Legends

Supplementary File Legend

References

Supplementary Experimental Procedures

Imaging

Imaging was performed on a Zeiss AxioObserver.Z1 inverted microscope with a (40x, 1.3NA) oil immersion objective and a (26mm WD, 0.55NA) condenser and a Lumencor Spectra X LED light engine for epifluorescence microscopy illumination. White LED light used for DIC microscopy was filtered with a 490 nm long-pass filter (Chroma) to avoid unnecessary exposure to short wavelength light. Images were captured with either a CCD camera (CoolSnap HQ Photometrics) or a scientific CMOS camera (Andor Zyla). We used a 0.63x demagnifying camera adapter except when imaging Y-cell-PDA-neuron transdifferentiation to achieve 0.26 $\mu\text{m}/\text{px}$ resolution or 0.16 $\mu\text{m}/\text{px}$ respectively. Capturing the entire chamber in a single frame at 0.26 $\mu\text{m}/\text{px}$ requires a camera sensor with at least 1550x1550 pixels.

Fluorescence intensity measurements

We performed analysis of fluorescence intensities (**Figures 4 & 6** in main manuscript) with custom-written MATLAB[®] scripts. Epifluorescence micrographs were median-filtered with a filter size of three pixels to reduce camera shot noise. To obtain fluorescence levels of a cell or nucleus, we first selected the z-slice in which the nucleus of the cell was in focus, based on the DIC micrographs. We then selected a region of interest (ROI) containing the cell, as well as a much larger region of the animal in which no cell expressed the reporter. We separated background and foreground in the ROI using Otsu thresholding (Otsu, 1979) and considered the convex hull of the foreground pixels as the outline of the cell/nucleus. Fluorescence was calculated as the average intensity in the cell region, subtracted by the average intensity of the background. If the effectiveness metric of the Otsu thresholding was smaller than 0.65, no fluorescence intensity was assigned.

Deconvolution and automated z-stack alignment

We measured the point spread function (PSF) of our optical setup using red (580/605nm) and green (505/515nm) fluorescent 200nm beads (ThermoFisher Scientific). With the obtained PSFs, we deconvolved fluorescence z-stacks using the classic maximum likelihood estimation (CMLE) algorithm with standard parameters

(refractive index of imaging medium: 1.338) in the Huygens Professional software (Huygens Essential 3.7.1) by Scientific Volume Imaging (SVI). We then straightened each three-dimensional image stack, based on an automatically detected backbone of the deconvolved GFP fluorescence signal (Peng et al., 2008) (**Figure 7B** in main manuscript). Backbones with high curvature indicated worms immobilized in a folded position and were excluded from further analysis because backbones could not be reliably extracted without manual corrections (~7%). We iteratively trained a pixel-based classifier (<http://ilastik.org/index.html>) on two straightened GFP z-stacks from a single early L3 and a mid-L4 animal until the probability maps were stable and adequately distinguished the nuclei from background and mitochondrial signal. Muscle cell nuclei positions were then detected from probability maps with an applied threshold through centroid detection of connected components. The same classifier was used to align all imaged worms (N = 18) without further re-training. We determined the anterior-posterior (AP) axis of the animal based on the greater accumulation of muscle cell nuclei around the head region. Since, both the GFP and the mCherry channels contained little information about the dorsal-ventral (DV) axis, we trained a support vector machine image classifier (MATLAB[®]) on 130 DIC frames of animals of all imaged larval stages (late L2 to mid-L4). This classifier was able to correctly estimate each animal's DV axis with 92% accuracy. Misclassified orientations were manually corrected. After AP-DV pre-alignment, subsequent stacks were aligned with a rigid body transformation estimated by an iterative closest point algorithm (**Figure 7C** in main manuscript) to obtain time lapse movies of PVD arborization (**Movie S4**). Source code can be provided upon request.

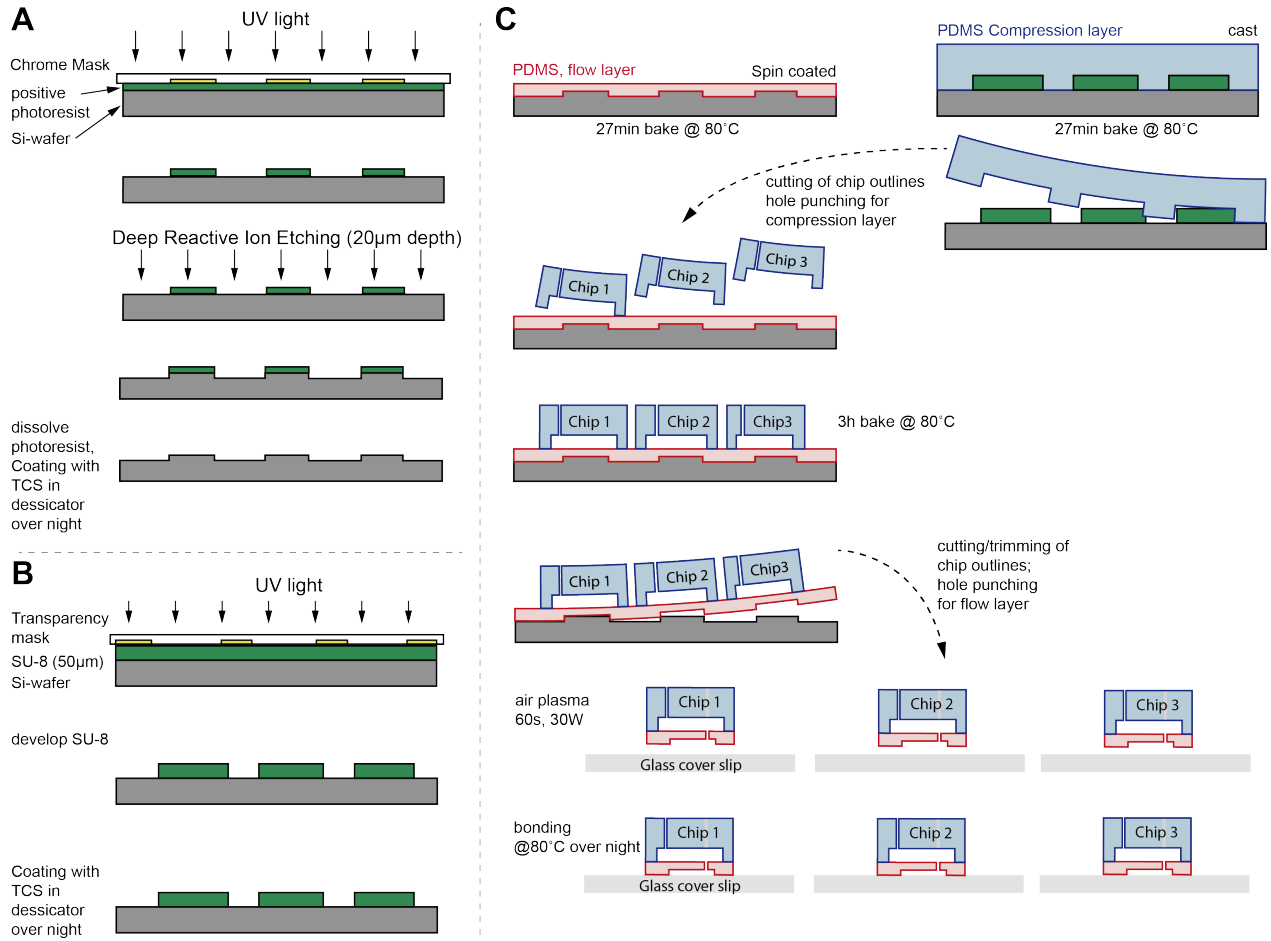


Figure S1. Illustration of the mold and chip fabrication processes. Heights of layers not drawn to scale. (A) Fabrication of the flow layer mold with deep reactive ion etching. (B) Fabrication of the compression layer with standard photolithography. The mold for the flow layer is fabricated with Deep Reactive Ion Etching (DRIE). The mold for compression layer is fabricated using standard photolithography. (C) Illustration of the fabrication process for the two-layer microfluidics device. See **Experimental Procedures** in main manuscript for details, related to Figure 1.

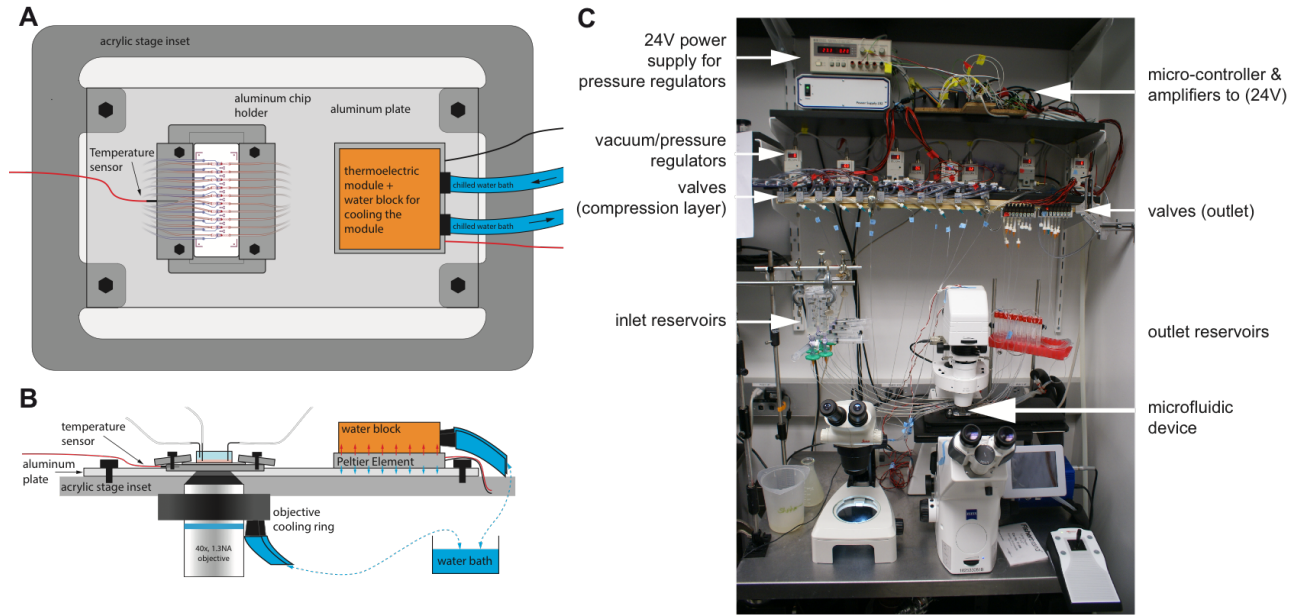


Figure S2. Temperature-controlled stage and setup. Top view (A) and side view (B) schematics of the temperature controlled stage used for imaging. AutoCad files and AutoDesk Inventor drawings for parts can be provided upon request. (C) Overview of the setup, related to Figure 1.

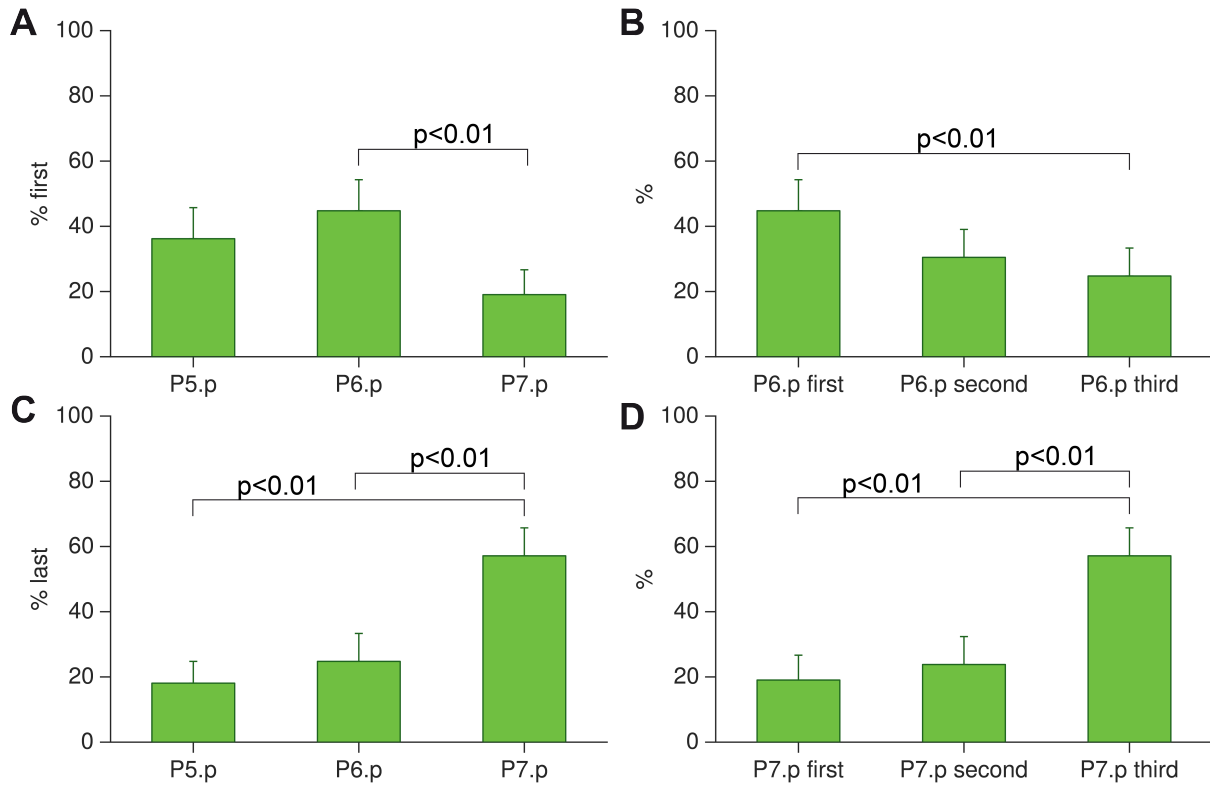


Figure S3. Statistics of division orders for the first VPC division (n=106 animals). (A) Percentage of animals in which P5.p, P6.p, or P7.p divided first. (B) Frequency of animals in which P6.p divided first, second or last. (C) Percentage of animals in which P5.p, P6.p, or P7.p divided last. (D) Frequency of animals in which P7.p divided first, second or last. P7.p is statistically significantly more likely to divide last among the vulval fate VPCs than P5.p and P6.p. All error bars indicate 95% confidence intervals of bootstrap distributions (10,000 bootstrap samples). p-values were computed from overlap of the bootstrap distributions, related to Figure 3.

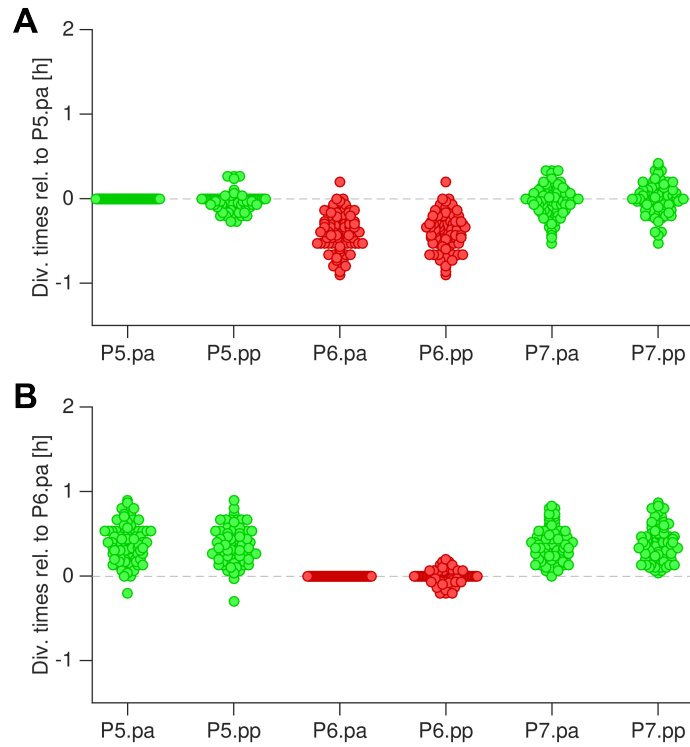


Figure S4. Relative division timings for the second VPC division (n=105 animals). (A) Time point of the second VPC division relative to the P5.pa division in each animal obtained by following divisions in the microfluidic device. Red (green) circles indicate division times for 1° (2°) fate cells. (B) As A but relative to the P6.pa division. Note that P6.p daughter divisions are highly synchronous and consistently before P5/7.p daughter divisions, related to Figure 3.

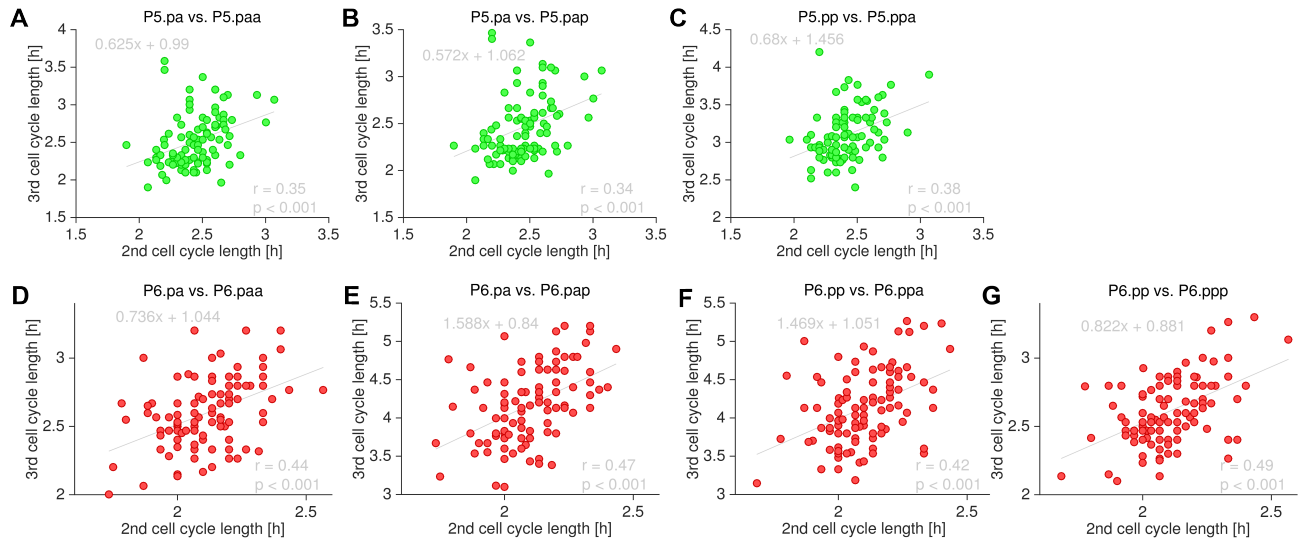


Figure S5. Correlations between second and third VPC cell cycle durations. (A-G) Scatter plots depicting the length of the second vs. third VPC cell cycle for P5.p and P6.p descendants. Gray lines indicate linear regression, $y = ax + b$. Fit parameters are given in gray on the upper left corner in each graph. Pearson correlation coefficient r and significance value p are given in the lower right corner in each graph. The length of second and third cell cycle is positively correlated in all P5.p and P7.p descendants, related to Figure 3.

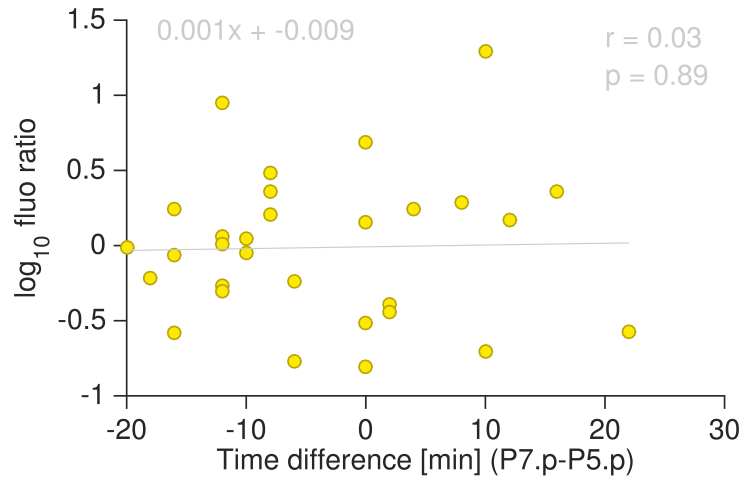


Figure S6. Relative timing of the first division of P7.p vs. P5.p vs. fluorescence intensity ratio of P7.p vs. P5.p in animals expressing *lst-5_{pro}::YFP*. Gray line indicates linear regression, $y = ax + b$. Fit parameters are given in gray on the upper left corner. Pearson correlation coefficient r and significance value p are given in the lower right. Time difference between the P7.p and P5.p division is uncorrelated with the ratio of their fluorescence intensities, related to Figure 4.

SUPPLEMENTARY MOVIE LEGENDS

Movie S1. Real-time movie taken during an immobilization procedure applied to an L2 animal in the microfluidic chamber, related to Figure 1.

Movie S2. Scoring of the first VPC division. Series of animated z-stacks of DIC micrographs of an immobilized L3 larva (from Figure 3 in the manuscript), showing vulval precursor cells P3.p-P7 during the P4.p division. Animated z-stacks are paused at the slice in which VPCs are in focus. 04h16min – prior to P4.p division. Nucleus and nucleolus of P4.p (red outline) are readily discernible; 04h24min – mitotic nuclear envelope breakdown. Nucleus and nucleolus of P4.p are no longer visible; 04h32min – cytokinesis. The cytokinetic furrow is apparent by the kink (note red outline); 04h40min – after division. Red outline indicates P4.p descendants, related to Figure 2.

Movie S3. Scoring of the transverse vulval divisions. Series of animated z-stacks of DIC micrographs of an immobilized L3 larva. Animated z-stacks are paused at the slice in which P6.ppp (red outline) or its descendants are in focus. 12h24min – prior to P6.ppp division. Late 4 cell stage vulva; 12h32min – the nucleolus of P6.ppp is no longer visible and the nucleus has undergone a characteristic rounding and widening compared to the other vulval cells; 12h40min – point of P6.ppp division. Outline of the P6.ppp nucleus is no longer visible; 12h56min – after P6.ppp division. Nuclei of P6.pppl/r (red outlines) become faintly apparent; 13h12min – Nuclei of P6.pppl/r (red outlines) are readily discernible, related to Figure 2.

Movie S4. Following PVD neurite outgrowth with automated alignment and segmentation of high-resolution three-channel z-stacks from the late L2 stage to mid L4 (24h). Time lapse movie of DIC (top row) and deconvolution (all other rows) micrographs after automated straightening and alignment; Top: Central z-section of DIC stacks. Upper middle, lower middle & bottom row: Maximum z-projections of the left side of the animal (10-15 z-slices). Green: *myo-3pro::GFP::LacZ::NLS* + *myo-3pro::mitochondrial GFP*; Magenta: *ser-2pro3::mCherry* Bottom row: Merged GFP and mCherry, related to Figure 7.

Movie S5. Initiation and pruning of PVD tertiary and quaternary branches. Maximum z-projection (12 slices) of time lapse deconvolution micrographs of a late L3 larva imaged every 60s with *ser-2pro3::mCherry* (48 z-slices, 0.7 μm spacing). Green (magenta) arrowheads indicate extending (retracting) branches. Note the two tertiary branches that retract after close contact. Also note that the new quaternary is initiated only after retraction of the tertiary branch is complete, related to Figure 7.

Movie S6. Initiation and pruning of PVD primary, secondary, tertiary and quaternary branches. Maximum z-projection (15 slices) of time lapse deconvolution micrographs of an early L3 larva imaged every 60s with *ser-2pro3::mCherry* (48 z-slices, 0.7 μm spacing). Green (magenta) arrowheads indicate extending (retracting) branches. Note the quaternary branch that is erroneously initiated ventrally around 130 min, pruned and then re-initiated on the dorsal side around 185 min, related to Figure 7.

SUPPLEMENTARY FILE LEGENDS

File S1. AutoCad file with the design of the microfluidic device, related to Experimental Procedures and Figure 1.

REFERENCES

Otsu, N. (1979). A threshold selection method from gray-level histograms. *IEEE Trans Systems Man Cybernet* 62–66.

Peng, H., Long, F., Liu, X., Kim, S.K., and Myers, E.W. (2008). Straightening *Caenorhabditis elegans* images. *Bioinformatics* 24, 234–242.